Review of Scientific Instruments

RESEARCH ARTICLE | SEPTEMBER 07 2023

The TU Wien Turbulent Water Channel: Flow control loop and three-dimensional reconstruction of anisotropic particle dynamics

Vlad Giurgiu ; Giuseppe Carlo Alp Caridi ; Mobin Alipour ; Marco De Paoli ; Alfredo Soldati

Rev. Sci. Instrum. 94, 095101 (2023)
https://doi.org/10.1063/5.0157490

AIP Publishing

Review of Scientific Instruments ARTICLE pubs.aip.org/aip/rsi

The TU Wien Turbulent Water Channel: Flow control loop and three-dimensional reconstruction of anisotropic particle dynamics

Cite as: Rev. Sci. Instrum. 94, 095101 (2023); doi: 10.1063/5.0157490
Submitted: 8 May 2023 • Accepted: 7 August 2023 •
Published Online: 7 September 2023

Vlad Giurgiu,[1] Giuseppe Carlo Alp Caridi,[1] Mobin Alipour,[1,2] Marco De Paoli,[1,3] and Alfredo Soldati[1,4,a)]

AFFILIATIONS

[1] Institute of Fluid Mechanics and Heat Transfer, TU Wien, 1060 Wien, Austria
[2] Department of Mechanical Engineering and Material Science, Yale University, New Haven, Connecticut 06511, USA
[3] Physics of Fluids Group, University of Twente, 7500AE Enschede, The Netherlands
[4] Polytechnic Department, University of Udine, 33100 Udine, Italy

[a)] **Author to whom correspondence should be addressed:** alfredo.soldati@tuwien.ac.at

ABSTRACT

A horizontal water channel facility was built to study particle dynamics in a turbulent flow. The channel is sufficiently long to produce fully developed turbulence at the test section, and the width-to-height ratio is sufficiently large to avoid the sidewall effect for a large proportion of the cross-section. The system was designed to study the dynamics of complex-shaped particles in wall-bounded turbulence, the characteristics of which can be finely controlled. A maximum bulk velocity of up to 0.8 m s^{-1} can be achieved, corresponding to a bulk Reynolds number of up to 7×10^4 (shear Reynolds number ≈1580), and flow parameters can be controlled within ±0.1%. The transparent channel design and aluminum structures allow easy optical access, which enables multiple laser and camera arrangements. With the current optical setup, a measurement volume of up to $54 \times 14 \times 54$ mm^3 can be imaged and reconstructed with six cameras from the top, bottom, and sides of the channel. Finally, the in-house developed reconstruction and tracking procedure allows us to measure the full motion of complex objects (i.e., shape reconstruction, translational, and rotational motions), and in this instance, it is applied to the case of microscopic, non-isotropic polyamide fibers.

I. INTRODUCTION

The dispersion of small particles in turbulent flows is a common unifying feature characterizing a number of environmental processes.[1] Among these processes, there is increased public concern about pollution due to microplastic particles in oceanic and other environmental flows.[2] These microplastic particles have complicated non-isotropic shapes, thus making modeling their dynamics more difficult. In this specific instance, of paramount importance to prevent pollution is the rate at which the particles are dispersed and transported by turbulence.[3,4] Particle transport and dispersion in turbulence are highly non-uniform and intermittent phenomena that depend on the local dynamics of turbulence structures[1] and on particle responses to fluid motions. In addition, when the particles are non-spherical in shape, extremely little is known about the forces exerted by the flow and, therefore, the resulting transport dynamics.[5]

To produce a homogeneous experimental dataset aimed at improving our knowledge of the fundamental dynamics of anisotropic particle transport in turbulence, the TU Wien Turbulent Water Channel was designed and built with the specific focus of understanding the dynamics of microplastics in the ocean. Microplastics are defined as fragments less than 5 mm in size and made from synthetic plastic materials such as polymethyl methacrylate (PMMA), polypropylene (PP), polystyrene (PS), polyethylene (PE), polyethylene terephthalate (PET), and others.[2] They originate from anthropogenic activities such as industrial or household processes[6] and are dispersed in the environment via natural pathways like rivers, oceanic currents, and air streams. Microplastic con-

tamination has been going on for decades and has been found in remote aquatic and terrestrial places such as the Kuril Kamchatka trench,[7] Mount Everest,[8] the oceans, and at the poles.[9] In the marine environment, microplastics are ingested by biota such as turtles, marine mammals, seabirds, and fish[10] and make their way through trophic transfer to humans,[2,11] where they may pose a health risk. The shape of these microplastics still demands appropriate classification,[12] but current findings support the evidence that the most abundant shape category (48.5%) of microplastics in water and sediment is fibers.[12] These anisotropic elongated microfibers, with a length distribution of around 1 mm and an aspect ratio of up to 1000,[12] can stay afloat on the surface and can also be transported to deep oceanic regions. However, modeling the dynamics of such anisotropic objects is complicated by their drag being only rarely colinear with the particle–fluid relative velocity and thus requires the derivation of a translational resistance tensor[5] that is not known for most practical instances.[13–18]

In this frame, experiments in turbulent channel flows play a key role: they allow optical measurements of fiber dynamics with no simplification of flow conditions. Determining experimentally the position and orientation of representative microplastics in environmental flows, i.e., millimeter-size objects that are relatively small compared to the flow structures, remains a challenging task. In this work, we aim precisely at this, and we present the TU Wien Turbulent Water Channel, a new facility specifically designed to investigate multiphase wall-bounded flows. Turbulent channel flow is an archetypal system to investigate the behavior of wall-bounded turbulent flows. The flow has a universal behavior that has been characterized over the last two centuries, although some features of this system remain elusive.[42] Currently, mature numerical techniques allow for the precise characterization of channel flows up to very large Reynolds numbers.[43] A number of recent experiments have been performed in this configuration. Turbulent bubbly flows in channel facilities have been investigated with optical techniques[25,35,37] in combination with heat transport.[38] The dynamics of spherical[24,26,27,29,30,36] and non-spherical[19–22,31,32,34] particles have also been investigated, both in free-surface and closed channel configurations as well as in turbulent pipe flows.[44] We refer to Table I for an overview of particle- and bubble-laden turbulent channel flow facilities, with an indication of the dimensions and shear Reynolds number considered.

The TU Wien Turbulent Water Channel is an optically accessible channel flow facility that can achieve bulk Reynolds numbers up to 7×10^4 (shear Reynolds number 1580). The flow is driven by gravity, can be seeded with anisotropic particles, and the channel can be used in an open (free-surface) or closed configuration. Particle tracking can be performed in different regions using non-invasive and non-intrusive optical techniques. In Sec. II, we present the experimental facility with hydrodynamic considerations, the control system, and the imaging system. In Sec. III, we present the flow measurements and compare the results against numerical simulations of channel and duct flows. An example of fiber measurement is presented in Sec. IV, and finally, a summary is discussed in Sec. V.

II. EXPERIMENTAL APPARATUS

The TU Wien Turbulent Water Channel has been designed to reproduce a fully developed turbulent field with fully benchmarked characteristics in which dispersed particles can be investigated. In the present context, the dispersed phase is constituted by

TABLE I. Overview of existing experimental water channel flow facilities used to investigate particle-laden flows. Channel configuration (open/closed), shear Reynolds number (Re_τ), facility location, and type of multiphase flows investigated (particles or bubbles) are indicated. Channel dimensions in streamwise (L), spanwise (W), and wall-normal (H) directions, as well as the channel aspect ratio (W/H), are explicitly reported.

References	Configuration	Re_τ (–)	H (mm)	W (mm)	L (mm)	W/H(–)	Location	Multiphase investigations
19 and 20	Open	110–170	···[a]	560	2 300	···	KTH (Stockholm, Sweden)	Rods
21	Open	400	≤130	360	3 660	···	Stanford University (Stanford, USA)	Rods
22 and 23	Open	570–620	≤150	150	1 400	···	U. Minnesota (Minneapolis, USA)	Spheres, disks, rods
24	Open	627–1924	≤280	300	18 600	···	U. Urbana-Champaign (Urbana, USA)	Spheres
25	Closed	147–260	40	400	2 000	10	The University of Tokyo (Tokyo, Japan)	Bubbles
26	Closed	172–208	40	400	2 000	10	U. Tokyo (Tokyo, Japan)	Spheres
27	Closed	187–225	50	50	5 000	1	KTH (Stockholm, Sweden)	Spheres
28 and 29	Closed	200–283	6	40	1 200	6.7	U. Alberta (Edmonton, Canada)	Spheres
30–32	Closed	435	50	50	2 550	1	Technion (Haifa, Israel)	Spheres, rods
33 and 34	Closed	530–785	20	200	1 000	10	La Sapienza University (Rome, Italy)	Rods
35	Closed	550	10	100	6 000	10	Hokkaido University (Sapporo, Japan)	Bubbles
36	Closed	570	4	36	488	9	U. Maryland (College Park, USA)	Spheres
37	Closed	1000[b]	15	100	3 000	6.7	NMRI (Tokyo, Japan)	Bubbles
38 and 39	Closed	70–2000[b]	40–80	300	1 000	3.8–7.5	U. Twente (Enschede, The Netherlands)	Bubbles
This facility[40,41]	Open/closed	180–1580	80	800	8 500	10	TU Wien (Vienna, Austria)	Curved fibers

[a]The fluid layer height is varied by changing the inclination of the channel.
[b]Estimated from the bulk Reynolds number, see (8).

anisotropic elongated particles that are almost neutrally buoyant, with the specific scope of determining the dynamical characteristics of microplastics in environmental flows, both in confined and free surface conditions. The height of the channel is 8 cm, which is large compared to the size of the microplastics (~5 mm) under investigation. To perform consistent, repeatable, and comparable experiments, two goals must be achieved: (i) statistical independence of the measurements from the geometrical features of the facility; and (ii) control of the main flow parameter, the shear Reynolds number. In this section, we describe how these targets are achieved.

This facility is composed of two subsystems: the main flow loop described in Sec. II A and the imaging system described in Sec. II C. In the following, we will describe the geometry of the channel with hydrodynamic considerations (Sec. II B), the control system (Sec. II D), the determination of the control parameters (Sec. II E), and the uncertainty on the Reynolds number (Sec. II F).

A. Main components of the system

A schematic representation of the TU Wien Turbulent Water Channel is provided in Fig. 1, where side [Fig. 1(a)] and top [Fig. 1(b)] views of the system are reported. The main components of the channel are the transparent duct, the upstream reservoir, and the downstream reservoir. The fluid is circulated from the downstream reservoir to the upstream reservoir by a pump (centrifugal volute Grundfos 100–160/176, maximum flow rate of 175 $m^3\ h^{-1}$), and the flow is subsequently driven by gravity. The upstream tank is made of stainless steel plates welded together. The downstream reservoir is made of polypropylene plates of 8, 10, and 12 mm thickness, which are welded together. The piping system is made of polyvinyl chloride (PVC) PN10 pipes with a 110 mm nominal diameter. The water is seeded with tracers and fibers in the downstream reservoir and pumped into the upstream reservoir. Fibers or particles are circulated with the fluid and, following the experiments, can be removed with the aid of a filter [see Fig. 1(b)] consisting of a sieve with a mesh size of 0.2 mm. To make the inflow uniform in the upstream reservoir, four circular openings are used as inlets. In addition, to minimize the fluctuations of the water level in the upstream tank, openings are equipped with valves that allow control of the flow in each inlet. A quantification of the remaining fluctuations is provided in Sec. II D.

The duct is made of transparent polymethyl-methacrylate (PMMA, 15 mm thick) to allow optical access. It is ~10 m long and is constructed by combining an inlet section, an outlet section, and four intermediate parts, each being 2 m long. The inner cross-section has dimensions of 800 × 80 mm^2 ($w \times 2h$, where h is the half-channel height). The channel is connected to the upstream and downstream tanks via a converging inlet and a 90° elbow, respectively. The top wall (cover) and the terminal section of the channel are equipped with air-release valves to serve the purpose of removing bubbles entrained during channel fill-up and trapped under the top wall. The upper wall of the channel is removable in all sections, and both open- and closed-channel experiments can be performed. In this study, we only consider the closed-channel configuration. The channel is supported by a metallic (ST27 steel) frame: Two legs (height 1200 mm) made of rectangular profiles are used in each section. This is sufficient to prevent deformations due to the channel and the water weight on the lower wall. To prevent deformation of the upper walls and increase the rigidity of the channel, each section cover is equipped with two PMMA cross beams. The choice of the particular geometrical features of the channel, such as entrance length and inner dimensions, is motivated by hydrodynamic considerations and discussed in Sec. II B. The imaging system, located 8500 mm downstream of the channel entrance, is described in detail in Sec. II C.

B. Geometry of the channel: Hydrodynamics considerations

To obtain a turbulent channel flow that is independent of duct geometry, two main geometrical parameters are considered: (i) the aspect ratio $\mathcal{AR} = w/(2h)$, which is important to evaluate potential effects of the sidewalls via secondary motions; and (ii) the entrance length, which is important to evaluate that a fully developed flow (i.e., streamwise invariance of relevant statistical quantities) is achieved before the test section. The TU Wien Turbulent Water Channel was designed to ensure that at the test section, the flow is fully turbulent and a significant proportion of the cross-section is free from sidewall effects.

Several works available in the literature investigated the influence of the side walls on the central (mid-span) plane of a duct or a boundary layer flow to determine the minimum value of the aspect ratio required to achieve velocity statistics that are independent of the presence of side walls. Bradshaw and Hellens[45] used a duct of $\mathcal{AR} = 5$ to study two-dimensional boundary layers, considering the negligible influence of the side-wall boundary layers on the measurements in the center. Dean[46] observed no consistent dependence of the aspect ratio on bulk quantities such as the skin friction factor for turbulent duct flows when $\mathcal{AR} \geq 7$. Zanoun, Durst, and Nagib[47] (duct $\mathcal{AR} = 12$) found good agreement between the friction factor measured from the pressure drop and the wall shear stress and the correlation given by Dean.[46] This supported the two-dimensionality of the flow. In an early work, Vinuesa, Schlatter, and Nagib[48] found that the local shear stress and centerline velocity became independent of the aspect ratio only for $\mathcal{AR} \geq 24$. However, they[49] later recognized the shortcomings of their previous study,[48] like the tripping quality and uncertainties in their measurements, and studied the decay rate of the kinetic energy of secondary structures generated by the side walls. They concluded that experimental turbulent duct flow facilities with an $\mathcal{AR} \geq 10$ can be compared with span-wise periodic numerical channels in terms of long-time statistical moments. With an $\mathcal{AR} = 10$, the TU Wien Turbulent Water Channel fulfills this criterion, and precise measurements of relevant statistics supporting this independence are reported in Sec. III C: profiles of the first and second order moments of the stream-wise velocity at four different proximities to the side-walls.

The entrance length, L_e, is the second hydrodynamic parameter taken into consideration for the statistical geometry-independence of the flow at the test section. Since the reference length scale commonly used for channel flows is the total height, $2h$, we consider here the dimensionless entry length defined as $L_e^* = L_e/(2h)$. Several studies have been conducted to identify the minimum value of L_e^* in different flow facilities. Laufer[50] measured turbulence statistics at the distance $L_e^* = 55$ from the entrance in a wind tunnel and considered the produced turbulent flow as fully developed. Dean[46] analyzed

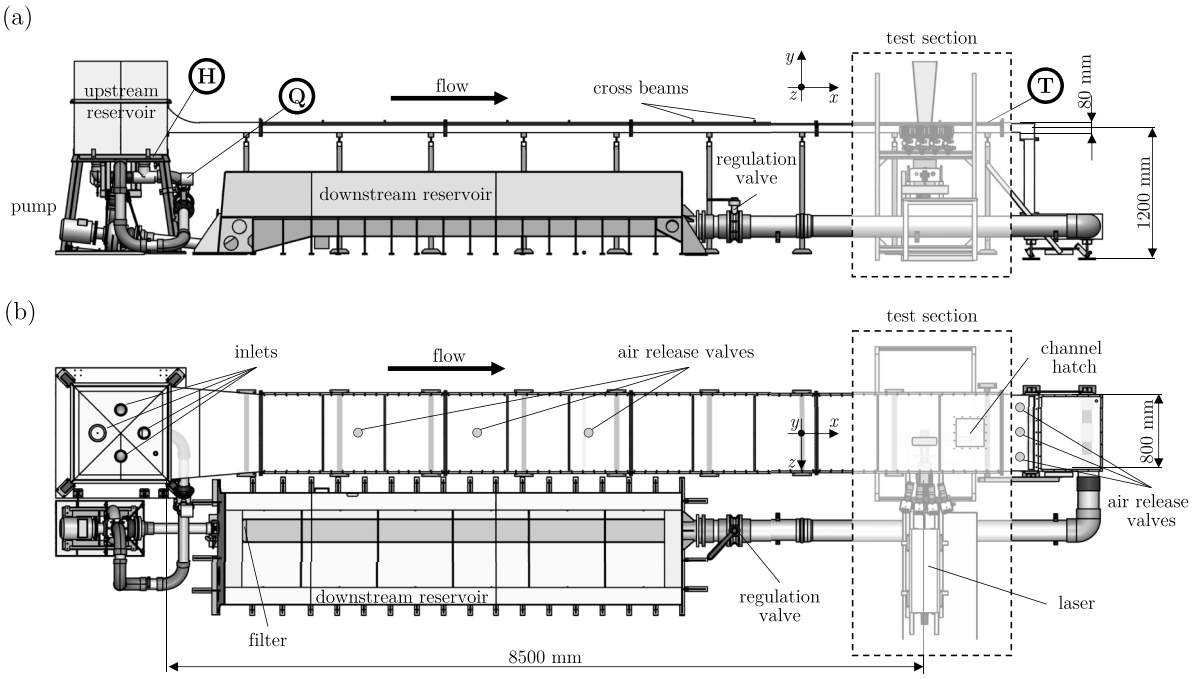

FIG. 1. Schematic representation of the TU Wien Turbulent Water Channel. Side (a) and top (b) views are reported. Main channel components and dimensions are indicated, as are the sensors of temperature (Ⓣ), water height in the upstream reservoir (Ⓗ), and flow rate (Ⓠ). The imaging system, located at the test section 8500 mm downstream of the channel entrance, is described in detail in Sec. II C. The coordinate system is also reported, indicating the streamwise (x), spanwise (z), and wall-normal (y) directions.

previous experimental studies on turbulent duct flows and observed that the entrance length used varied from $L_e^* = 23$ to over 300. Moreover, they noted the absence of precise details about the influence of entrance length in many of the reviewed works. Based on Pitot static tube measurements of the mean velocity, Lien *et al.*[51] recommended an entrance length $L_e^* \approx 130 - 150$. After decades of discussion on the necessary length between the flow entrance and measurement section, Doherty *et al.*[52] considered two criteria for determining if a turbulent flow is developed: (i) the streamwise invariance of statistical quantities, such as moments up to the fourth order, and (ii) the streamwise invariance of pre-multiplied energy spectra as indicators for flow structures. For turbulent pipe flows, they found that a development length of 184 diameters (D) is required to satisfy both criteria. The mean velocity converged at a distance greater or equal to $50 \times D$ and at higher momenta after $80 \times D$. Our measurement section is located ≈8.5 m away from the entrance, which is equivalent to $L_e^* \approx 105$. Although the entrance length does not strictly satisfy the criterion (ii) on the streamwise invariance of pre-multiplied energy spectra, our channel is in fair agreement with the values of L_e^* prescribed by Lien *et al.*[51] and Doherty *et al.*[52] to achieve streamwise invariance of statistical quantities up to the fourth order, and it has been designed with the maximum available space in the laboratory.

To further confirm that the flow achieved is independent of the geometry of the facility, in Sec. III, we will provide evidence of agreement of our measurements with numerical results in duct flows (i.e., with periodic boundary conditions employed in the numerical simulations in streamwise direction) and also with numerical channels (i.e., with periodic boundary conditions in both streamwise and spanwise directions).

C. Imaging system

The main components of the measurement system are the acquisition system—six high-speed Phantom VEO 340L cameras; the illumination system—a dual-cavity Nd:YAG Litron LD25-527 particle image velocimetry (PIV) laser; and the data processing system—a computer running the softwares DaVis 10.2.1 and MATLAB R2018B. The light emission is synchronized with the imaging system through a LaVision Programmable Timing Unit X (PTU X). The structures holding the laser and cameras are made out of aluminum profiles. The cameras are placed on Manfrotto 410 geared heads, which allow for three-angle adjustments. These are translated on carriers connected to optical X95 rails.

The initial image-to-volume calibration of the cameras is performed using a three dimensional LaVision 058-5 calibration plate, schematically represented in Fig. 2(a). The plate is inserted in the filled channel through the channel hatch, which is downstream of the measurement region [Fig. 1(b)]. A triangular ruler is used to align it with the side-wall. Before calibration, the air trapped between the water and the top channel wall is removed so that the images used for calibration are acquired in the same conditions as during experiments.

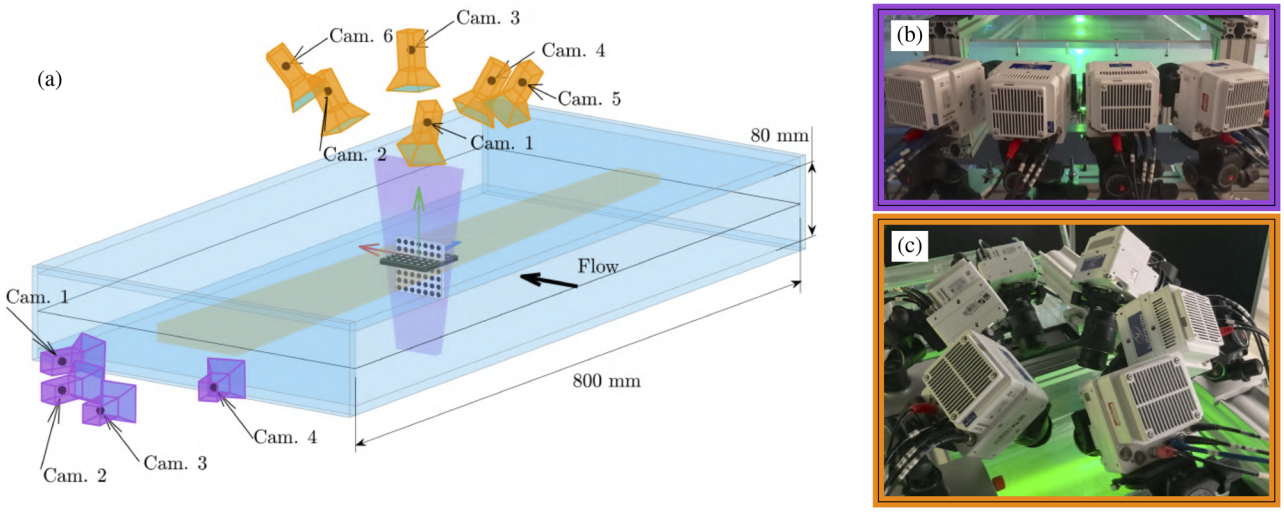

FIG. 2. Examples of camera configurations employed. (a) Sketch of the measurement section with cameras arranged in *lateral* (violet) and *span-wise* (orange) configurations, with the corresponding illumination volumes. The laboratory coordinate system is indicated by the red (stream-wise), blue (span-wise), and green (wall-normal) vectors. The transparent plane delimited by the black lines represents the channel's mid-height plane. Calibration targets (LaVision 058-5, markers not to scale) are also reported. Panels (b) and (c) show photographs of the four camera *lateral* configuration and the six camera *span-wise* configuration, respectively.

The design of the facility enables multiple camera setups. Cameras have been set up in the following ways: (i) *lateral* configuration, where 1 to 6 cameras are placed sideways with respect to the channel, viewing the measurement volume through the lateral walls [Fig. 2(b)]. This arrangement is used to perform 2D particle image velocimetry (PIV) measurements using one camera and 3D particle tracking velocimetry (PTV) measurements using multiple cameras, with cameras placed in a linear configuration.[40,41,53–58] (ii) *Span-wise* configuration, where 2 to 6 cameras are placed either above [Fig. 2(c)] or below (not shown) the channel and point at the measurement volume in a cross-like configuration.[53,57,59–67] This arrangement is suitable for particle tracking velocimetry (PTV) measurements.

D. Shear Reynolds number control system

Initial experimental campaigns have shown that long observation times ranging up to 3 h are necessary to obtain convergent higher order statistics. This is the case for three-dimensional flow measurements in which Shake-The-Box[68] is performed or for tracking anisotropic particles. Shake-The-Box is a particle-tracking method in which several frames (typically at least 50–100) are used to track the particles and determine their trajectories, which are subsequently employed to compute the three flow velocity components within the measurement region. We defined each group of consecutive frames as a *cycle*. To improve the convergence of the velocity statistics, uncorrelated cycles are recorded. The recording time of each cycle is short (typically less than a second). However, after recording each cycle, the images are transferred from the cameras to the workstation (duration: ≈1 min per cycle), and the acquisition continues with the following cycle. As a result, the recording time corresponding to a few hundred cycles may take a few hours. The same applies to anisotropic particles: a few hundred fiber images are collected to perform the tracking and to determine the fibers' position and dynamics. To improve the statistical convergence, uncorrelated cycles are collected and processed, with a corresponding recording/transfer time that may take a few hours. In this long period of time, ambient conditions could influence the repeatability of the experiments. To maintain the flow parameter, the shear Reynolds number, a flow control system is needed. In this section, we analyze the temporal evolution of flow variables during an experiment and describe the components and parameters of the control system.

The controlled variable is the shear Reynolds number, defined as

$$Re_\tau = \frac{hu_\tau}{\nu}, \tag{1}$$

where h is the duct inner half height and ν is the temperature-dependent kinematic fluid viscosity. The shear velocity u_τ is defined as $u_\tau = \sqrt{\tau/\rho}$, with τ being the shear stress generated at the solid wall by the fluid motion and ρ being the fluid density. The fluid temperature, θ, increases during experiments due to heat exchange with the ambient and viscous losses. The control system acts to approach the desired Re_τ, accounting for instantaneous variations of water properties due to temperature changes. Note that Re_τ cannot be directly measured with this system; therefore, it has to be inferred from the flow-rate and fluid viscosity, as discussed in detail in Sec. II E.

To achieve shear Reynolds number control, input sensors are required to monitor the status of the flow together with an output signal to manipulate the flow state. The input sensors are shown in Fig. 1(a) and include sensors for temperature (Ⓣ), pressure head (equivalent to the water height) in the upstream reservoir (Ⓗ), and flow rate (Ⓠ). The output is a voltage signal, which controls the pump.

We use a Silectron Sistemi SSR040SD2-4 frequency inverter to regulate the pump. The control system is implemented in LABVIEW 2019. The flow rate is measured by a Proline Promag 10D 100 mm electromagnetic flow meter [Ⓠ in Fig. 1(a)]. The flow rate measurement is accurate within ±0.75% of the reading value. An RS PRO Pt100 temperature probe [Ⓣ in Fig. 1(a)] is located 500 mm downstream from the measurement location and is used to measure the water temperature, θ. In addition, we also use a 300TX signal transmitter, which has been calibrated within ±0.29 °C with a Thermo Scientific AC200 device between 4.5 and 32 °C. The value of the water kinematic viscosity, ν, is approximated based on the measured temperature. A linear fit between values reported in Kind and Martin[69] for pure water is used. Finally, an RS PRO 828–5710 pressure sensor [Ⓗ in Fig. 1(a)] is used to measure the pressure head in the upstream reservoir. The signal is used to prevent overflow, to ensure that the water level is above the channel upper wall during the experiments, and during the phase preliminary to each experiment, when a sufficient water level has to be reached to facilitate camera calibration by submerging the calibration target. The water level signal has no influence on the flow control during the active phase of the experiments, i.e., image capture. Moreover, this signal is used to estimate the water level fluctuations in the upstream tank. At a fixed pump voltage generating a flow-rate of 267 l min^{-1}, we found these fluctuations to be ~0.1% of the height difference between the open surfaces of the two reservoirs.

To show the influence of the control system, in Fig. 3, we report measurements obtained from the sensors for four experiments, each lasting 3 h, with the control system active and inactive. The sensor readings are reported in Fig. 3(a)—real-time computed shear Reynolds number; Fig. 3(b)—temperature; and Fig. 3(c)—flow-rate. The colored data points (blue, red, and green) were recorded with the control system inactive, and correspondingly, the inverter voltage was set constant. The black data points in the same figure are readings with the control system active. Larger flow rates produce higher viscous losses that result in higher fluid temperatures; e.g., for $\langle Re_\tau \rangle = 720$ at $\langle \theta \rangle = 19.1$ °C, the heating rate is ≈0.27°C h^{-1}, which is equivalent to ≈930 W of heating power. This is the consequence of heat exchange with the environment and viscous losses in the pump, piping, and regulation valve. This effect can be observed in Fig. 3(a), where the higher the Re_τ, the higher the measured fluid heating rates. Note that for similar flow conditions, e.g., $Re_\tau = 719$ without control (green) and $Re_\tau = 720$ with control (black), the heating rates can be different due to different environmental conditions. The increase in temperature over time produces a decrease in fluid kinematic viscosity. Water properties as functions of temperature were evaluated[69] at a pressure of 1 bar: e.g., for an increase in temperature of 0.6 °C from 19.4 °C, a reduction of 1.5% of fluid viscosity is expected. Between the reported values, linear interpolation has been used. Due to the prohibitive costs associated with the large volume of water required (~3000 l), demineralized water was not employed, and tap water was used for all the experiments. For simplicity, tap water's properties were assumed to match those of pure water. The decrease in viscosity has a direct effect on Re_τ [Fig. 3(a)]: decreasing kinematic viscosity at constant flow rates produces an increase in Re_τ, e.g., for the measurement without control at $Re_\tau = 719$, the shear Reynolds number increases by ≈1% of the initial value over a period of 3 h. For an initial $Re_\tau = 358$ without control, an increase of ≈0.5% is observed

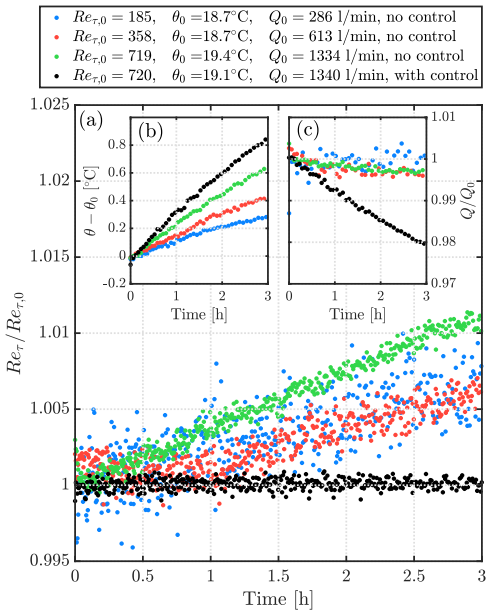

FIG. 3. Temporal evolution of sensor readings in four different experiments. Shear Reynolds number normalized with respect to the initial value is shown in (a). The temperature difference and volume flow rate divided by the corresponding initial values are shown in (b) and (c), respectively. All data have been filtered with a low pass Butterworth (LPBW) filter of third order with a cutoff frequency of 20 mHz and down-sampled to 1/20 Hz in (a) and 1/200 Hz in (b) and (c) for visualization purposes.

over the same period of time. To offset this error, the control system was engaged in a new experiment with similar initial flow conditions. The black data points in Fig. 3(a) correspond to the evolution of Re_τ over a 3 h period with the control system engaged, and we observe that the shear Reynolds number remains constant within ±0.1%. Similar to the uncontrolled measurements, the temperature shows a comparable increase over time [Fig. 3(b)]. Figure 3(c) shows a decrease of 2% in flow rate for the controlled measurements. This is expected since the control system is designed to compensate for the increase in Re_τ due to the decrease in viscosity by decreasing the flow rate. Note that for this measurement (black dots), the environmental temperature was higher than for the $Re_\tau = 719$ without control (green dots in Fig. 3), so a higher temperature increase is expected.

Finally, we describe the control algorithm. The process variable (y) is the shear Reynolds number computed from the measured variables: temperature (Ⓣ) and volumetric flow rate (Ⓠ). Note that the correlation (8), extensively discussed in Sec. II E, is used to estimate the Re_τ from the bulk Reynolds number, Re_{2h}. The difference between the set-point value (w), i.e., the desired value $(Re_{\tau,d})$, and the process variable (y), i.e., the measured value $(Re_{\tau,m})$, is the error (e). Provided that a digital technology is used for the control system, the equations are discretized with the current time, being $t_k = k \times \Delta T$, with ΔT being the time interval between two consecutive acquisitions and k the instant number. The manipulated process

variable (u) is the inverter control voltage, which consists of three components,

$$u_k = u_{P,k} + u_{I,k} + u_{D,k}, \tag{2}$$

defined as proportional (P), integral (I), and derivative (D). The proportional component

$$u_{P,k} = K_c e_k, \tag{3}$$

includes the action parameter (K_c), which defines how strongly the manipulated variable (u) responds to the current error (e). The integral part

$$u_{I,k} = u_{I,k-1} + \frac{K_c}{T_i}\left(\frac{e_k + e_{k-1}}{2}\right)\Delta T, \tag{4}$$

includes the time T_i that defines the contribution of the integrated error to u. Here, a trapezoidal approximation has been employed in Eq. (4). Finally, the derivative component

$$u_{D,k} = -K_c \frac{T_d}{\Delta T}[y_k - y_{k-1}], \tag{5}$$

with the derivative time, T_d defines the contribution of the temporal variation of the process variable (y) on u. Therefore, the manipulated variable can be computed[70] from Eq. (2) with the contributions defined in Eqs. (3)–(5).

The proportional integral differential (PID) parameters (reported in Table II) have been found through an auto-tuning relay procedure[71] implemented in the *PID Autotuning VI* algorithm[70] included with LabVIEW 2019 at an operating point of $Re_\tau \approx 360$, a water level of ≈460 mm, $\theta \approx 13\,^\circ$C, and a regulation valve (see Fig. 1) opened at 30°. To measure the response time of the shear Reynolds number control system (T_r), we performed a step response test: after a steady controlled condition at $Re_\tau = 360$ had been achieved, the set-point shear Reynolds number was suddenly increased to 390. We recorded the real-time shear Reynolds number. After $T_r = 8$ min, the measured shear Reynolds number settled within 0.5% of the final value of 390. We consider this response sufficiently fast because, without the control system, a shear Reynolds number increase from 360 to 390 due to a temperature increase would be achieved in ≈12 h [extrapolating the red dots in Fig. 3(a)]. The raw flow-rate and temperature voltage signals have been pre-filtered with an analog low pass filter with a cutoff frequency of 5 Hz to reduce environmental electromagnetic noise. Further filtering has been achieved digitally with low-pass Butterworth third order filters in LabVIEW 2019. The cutoff frequencies $f_{cut,\theta}$ and $f_{cut,Q}$ for the temperature Ⓣ and flow-rate Ⓠ sensors, respectively, are reported in Table II.

The control system also enables the safe operation of the facility. The safety system is composed of two subsystems: (i) an automatic detection of unsafe operation conditions, where the control program shuts down the pump if the water level exceeds 600 mm; and (ii) a checklist for the operator to complete before starting the system.

E. Determination of the shear Reynolds number

In wall-bounded turbulence, the shear Reynolds number (Re_τ) is the quantity that is generally used to make reliable comparisons between experiments and direct numerical simulations (DNSs), and it is defined in Eq. (1). Measuring and imposing the shear velocity (and then the Reynolds number) in the TU Wien Turbulent Water Channel is not trivial. Due to the large size of the facility, the small pressure drop along the channel makes accurate measurements hard to obtain. In addition, the most natural parameter to be controlled in this configuration is the bulk Reynolds number. As a result, of primary importance to obtain a given value of shear Reynolds number is the determination of the duct friction factor, which relates the shear stress at the walls to the bulk velocity, or in other words, the shear and bulk Reynolds numbers. For that purpose, a widely used approach consists of assuming that the same friction relationship can be used as for flows in circular pipes, provided the Reynolds number is defined based on a convenient duct length scale.[72] The length scale traditionally used is the hydraulic diameter,[73] $D_h = 4A/P$, where A is the flow cross-section and P is the wetted perimeter, and the bulk Reynolds number for a rectangular duct can be written as

$$Re_{D_h} = \frac{4hw\langle u\rangle}{(2h + w)\nu}, \tag{6}$$

where w and $2h$ are the duct inner width and height, and ν is the kinematic viscosity. The mean stream-wise flow velocity (or bulk velocity) $\langle u\rangle$ is the parameter that can be controlled, and it is related to the flow rate Q (measured via the flow meter, Ⓠ) through the channel cross-section, $A = 2h \times w = 80 \times 800\ \text{mm}^2$ (height × width). As a result, the bulk velocity is computed as $\langle u\rangle = Q/A$. A collection of results of shear and bulk Reynolds numbers obtained in duct and channel flows, both experimentally and numerically, is shown in Fig. 4(a), where the bulk Reynolds number is based on the channel/duct height,

$$Re_{2h} = \frac{2h\langle u\rangle}{\nu}. \tag{7}$$

The data are well fitted by the correlation proposed by Pope,[74]

$$Re_\tau = 0.09 \times Re_{2h}^{0.88}, \tag{8}$$

which is inverted to compute the bulk Reynolds number

$$Re_{2h,P} = 15.43 \times Re_\tau^{1.1364}, \tag{9}$$

TABLE II. Summary of control system parameters: PID values, response time, and filtering specifications. All parameters are discussed in detail in Sec. II D.

Parameter	Symbol	Value	Units
Sampling time	ΔT	0.1	s
Proportional gain	K_c	0.001	···
Integral time	T_i	15	s
Derivative time	T_d	0.6	s
Response time	T_r	8	min
Sensor Ⓣ filter type	···	LPBW[a]	···
Sensor Ⓣ filter cutoff freq.	$f_{cut,\theta}$	0.1	Hz
Sensor Ⓠ filter type	···	LPBW[a]	···
Sensor Ⓠ filter cutoff freq.	$f_{cut,Q}$	0.1	Hz

[a]Low-pass Butterworth third order.

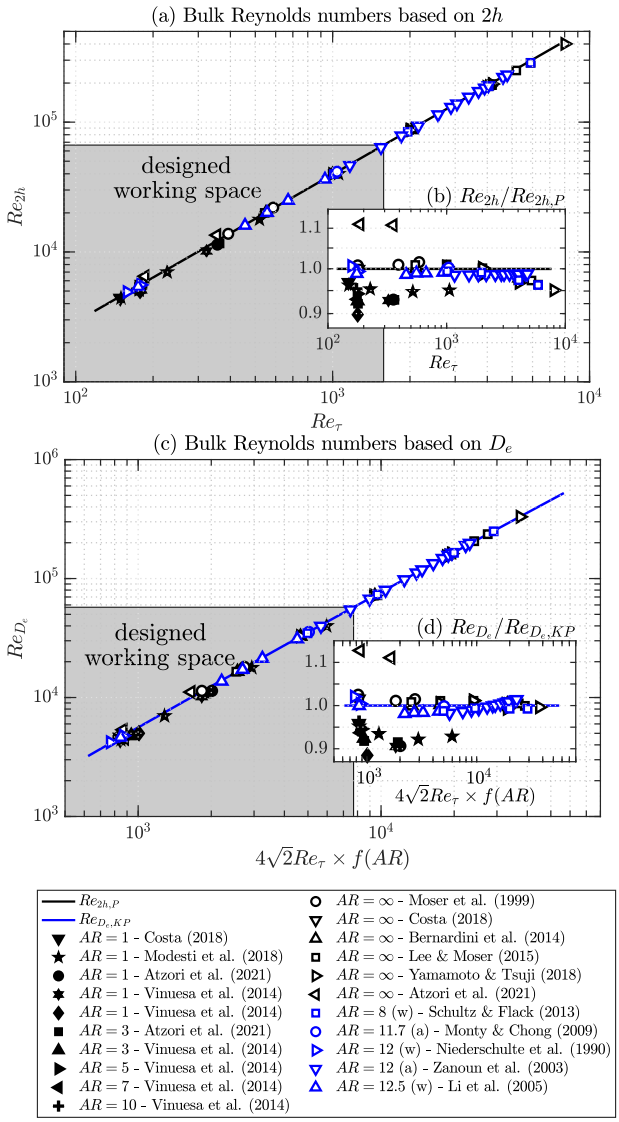

FIG. 4. Bulk and shear Reynolds numbers. The designed working space of the present facility is indicated by the shaded region. Results are reported for several numerical (black symbols) and experimental (blue symbols) facilities with different aspect ratio $(\mathcal{AR})$. Experiments[47,75–78] consist of measurements in air and water ducts, respectively indicated with *a* and *w*. Simulation results for channels[43,79–83] and ducts[79,83–85] are reported. (a) Bulk Reynolds number based on the channel height (Re_{2h}) against shear Reynolds number (Re_τ). Correlation (9) provided by Pope[74] is also shown (black solid line). (b) Relative uncertainty of the value of the shear Reynolds number predicted $(Re_{2h,P})$ compared to the value measured (Re_{2h}). (c) Bulk Reynolds number based on the effective diameter (Re_{D_e}) against the shear Reynolds number multiplied by a corrective factor accounting for the geometry of the facility $[4\sqrt{2}f(\mathcal{AR})$, see Eq. (10)]. The Karman–Prandtl friction law (11) provided by Pirozzoli[72] is also shown (blue solid line). (d) Relative uncertainty of the value of the shear Reynolds number predicted $(Re_{D_e,KP})$ compared to the value measured (Re_{D_e}).

corresponding to the desired value of Re_τ. In this work, we will use (8) to correlate bulk and shear Reynolds numbers, and we will verify the accuracy of this approach in Sec. III B. The design working space of the TU Wien Turbulent Water Channel is indicated in gray in Fig. 4(a). It is obtained considering the maximum pump flow rate (175 $m^3\ h^{-1}$) at a temperature of 24 °C, which gives Reynolds numbers corresponding to a bulk value of Re_{2h} = 66 547 and a shear Reynolds value of Re_τ = 1580.

One can observe in Fig. 4(b) that the difference between the desired value of shear Reynolds number and the value predicted by the correlation can exceed 5% of Re_τ, especially in the instance of large values of bulk Reynolds number ($Re_\tau > 3000$). Therefore, in the following, we provide an alternative formulation that can be used in the instance of large shear Reynolds numbers to estimate Re_τ from the bulk Reynolds number.

Pirozzoli[72] has shown that the predictions obtained with the hydraulic diameter are less accurate in the presence of ducts with large aspect ratio, $\mathcal{AR}$, being $\mathcal{AR} = w/(2h)$. A more accurate and physically grounded representation of the friction factor is obtained when the flow is characterized by the effective diameter,[72]

$$D_e = D_h \frac{1+\mathcal{AR}}{2\mathcal{AR}} e^{\frac{\mathcal{AR}-1}{2\mathcal{AR}}} = D_h f(\mathcal{AR}), \tag{10}$$

with $f(\mathcal{AR}) = (1+\mathcal{AR})/(2\mathcal{AR}) \exp[(\mathcal{AR}-1)/(2\mathcal{AR})]$. The definition (10) returns $D_e = D_h$ for square ducts $(\mathcal{AR} = 1)$, whereas $D_e = (\sqrt{e}/2)D_h$ for channels (numerical simulations with spanwise-periodic boundary conditions, $\mathcal{AR} \to \infty$). Modeling the friction factor with the Karman–Prandtl (KP) friction law for circular pipes,[72] one can relate the bulk Reynolds number based on the effective diameter (Re_{D_e}), the shear Reynolds number (Re_τ), and the domain geometry, $f(\mathcal{AR})$. Using the same set of data analyzed in Figs. 4(a) and 4(b), we obtain that the correlation

$$Re_{D_e,KP}(Re_\tau, \mathcal{AR}) = \left(4\sqrt{2}Re_\tau \times f(\mathcal{AR})\right) \times \left[2.076 \times \log_{10}\left(4\sqrt{2}Re_\tau \times f(\mathcal{AR})\right) - 0.621\right] \tag{11}$$

fits well the data, as shown in Fig. 4(c). The discrepancy between the predicted value of bulk Reynolds number ($Re_{D_e,KP}$, blue solid line), obtained using the Karman–Prandtl friction law via Eq. (11), and the measured value (Re_{D_e}), is much smaller in this case, in particular at large Reynolds $(Re_\tau > 3000)$ and large aspect ratios (channels). The discrepancy existing between the predicted value and the actual value exhibited from numerical simulations of ducts at small Re_{D_e} can be as high as 9%.

F. Reynolds number uncertainty

To estimate the uncertainty in the main parameter of the facility,we followed the procedure described by Moffat.[86] The uncertainty of the bulk Reynolds number (Re_{2h}) is influenced by temperature (θ), flow rate (Q), and channel inner width (w) measurements.

We consider a measurement lasting 3 h with the control system engaged at $Re_{2h} = 27\,249$ (corresponding to $Re_\tau = 720$ in Fig. 3—black points). During the measurement, the water height in the upstream reservoir was reduced by 35 mm, which is equivalent to ≈0.2 l min^{-1}. This corresponds to ≈0.015% of the initial flow rate of 1340 l min^{-1}. Therefore, the true value of the flow rate through the channel is considered to be the one through the flow meter (Ⓠ). The true value of the temperature measurement is considered to be the temperature of the probe (Ⓣ). This assumes an infinite heat transfer coefficient between the water and the probe and the ideal thermal isolation of the probe.

Temperature and flow rate sensors have been calibrated with an end-to-end procedure.[86] For the temperature calibration, the probe was submerged in the Thermo Scientific AC200 immersion circulator. This produced 12 different temperatures equally spaced between 4.5 and 32 °C. The readings of the voltage for each set point have been collected, and between these values, a linear interpolation has been used. During the calibration, the flow rate sensor was set to simulation mode,[87] where a flow rate value can be set on the sensors' screen and the corresponding voltage value is read on the computer. From the pairs of flow rate input values and read voltage values, a calibration table is compiled and used in the control system. Between the values, a linear interpolation has been used.

The multiple-sample uncertainty analysis[86] on the bulk Reynolds number (Re_{2h}) yields a bias limit (B), i.e., an estimate of the maximum probable value of the fixed error, and a precision index (S), i.e., an estimate of the random errors. Variable errors in the calibration procedure have been fossilized in the bias limit[86] to simplify the uncertainty estimation. To compute the random error estimate, N independent samples were collected. Consequently, the number of degrees of freedom is $N - 1$. To estimate the likely limits of a future mean, the Student's t distribution at x% confidence level, indicated as $t_{100\%-x,N-1}$, has been used. The best estimate of the bulk Reynolds number is[86]

$$Re_{2h} \pm \sqrt{B^2 + (tS)^2}, \tag{12}$$

where Re_{2h} is the mean bulk Reynolds number during the experiment. The results are summarized in Table III.

III. FLOW MEASUREMENTS

A. Midspan measurements

The flow measurements are performed in correspondence with three values of Re_τ, namely 187, 368, and 726 at the channel midspan ($z = 0$). The flow scales are listed in Table IV. The measurement configuration, consisting of a planar PIV, features the camera and light source presented in Sec. II C. Every pair of frames is acquired with a delay time of 1 s using *recording-loop* mode (LaVision DaVis 10.2.1 software) in order to ensure the convergence of the turbulent quantities with the high-speed PIV system. The total number of pairs is 2500. The time interval between the first and second frames is set to 4, 2, and 1 ms, corresponding to the increasing Re_τ, in order to ensure a particle displacement of ~12 pixels at the outer layer at each Re_τ. The imaging settings and the tracers' properties are reported in Table IV. Raw images are pre-processed by applying a sliding minimum subtraction (kernel of 13 time-steps) and a spatial normalization with a local average (computed with 100 × 100 pixels). An example of a pre-processed image corresponding to the experiment $Re_\tau = 187$ is shown in Fig. 5.

The velocity fields are obtained using the software PaIRS-UniNa 0.1.2.[88–90] A final interrogation window of 16× 16 pixels, corresponding to a squared window of side 0.67 mm, with 75% overlapping, yielded a vector grid dimension of 400× 120 with 0.16 mm as vector pitch. The size of the final interrogation window ensures the presence of 6 to 8 seeding particles, as shown by the green box in Fig. 5(c). The final profiles, an example of which in the near-wall region is shown in Fig. 5(b), are then obtained by averaging the velocity along the streamwise direction (x) and in time.

The results of the PIV measurements are compared against numerical simulations[91] obtained using a spectral method.[92] The profiles of the mean velocity non-dimensionalized by the wall-shear velocity, u_τ, are shown in Fig. 6. Experiments performed are in agreement with DNS data for all values of Re_τ considered, from the center of the channel (logarithmic region) up to the viscous sublayer, $y/l_\nu < 5$, being $l_\nu = h/Re_\tau$. At the present magnification, the spatial resolution allows only one data point in the sublayer at $Re_\tau = 726$. It is worth mentioning that if higher resolution is needed, the measurements can be performed with a larger magnification, which can reach up to ~1 with *macro* lenses. The uncertainty quantification of the velocity measurements is performed using the particle disparity method.[93,94] Technically, particle disparity is an *a posteriori* method that quantifies the uncertainty of the measured particle image displacement considering the contribution of individual particle images to the cross-correlation peak. The uncertainty of the mean velocity is shown in Fig. 6(a) as error bars and, for clarity, also in Fig. 6(b). The region close to the wall experiences the largest uncertainties, especially for larger Re_τ, due to the velocity gradients, i.e., 15%–20% of the mean velocity, while in the outer layer, $\varepsilon_{\langle u\rangle}/\langle u\rangle$ is reduced to less than 1%. We show in Fig. 7 the Reynolds-stress profiles expressed in wall units, i.e., normalized by the shear velocity u_τ. In agreement with the DNS data, the peaks of the $\langle u'u'\rangle/u_\tau^2$ profiles are located at $y/l_\nu \approx 14$. The spanwise and shear components of the measured Reynolds stresses are also in good agreement with the DNS data. The uncertainties of the Reynolds-stresses are computed from the propagation of the velocity uncertainties using the expression derived by Sciacchitano and Wieneke.[95] The profiles of the normalized uncertainty, $\varepsilon_{\langle u_i'' u_j''\rangle}/u_\tau^2$, are shown in Figs. 7(b)–7(d) for the three components of the Reynolds stresses. Finally, we report in Fig. 8 the data on skewness and flatness (streamwise components). We observe that, in this case, the trend is also captured by the PIV results. However, a small discrepancy is observed, suggesting that perhaps a statistical convergence of this high-order statistics may not yet be fully achieved. The uncertainty of skewness and flatness, reported as error bars in Fig. 8(a) and more in detail in Figs. 8(b) and 8(c), is evaluated considering the statistical convergence, i.e., computing the standard deviation of the data when the largest fluctuations end (in this case after 800 samples).[96]

B. *A-posteriori* verification of the shear velocity

We have described in Sec. II D the control system employed, which is designed to run the system at the desired shear Reynolds number. Unlike the bulk velocity, which is directly measured by the

TABLE III. Multiple-sample uncertainty estimate[86] of the bulk Reynolds number (Re_{2h}). The shear Reynolds number (Re_τ) and corresponding uncertainty were computed with correlation (8). Fixed errors for the flow rate (Q), temperature (θ), and channel width (w) are reported for a 95% confidence level. The bias limit (B), precision index (S), and Student's distribution for 1001 independent samples at the 95% confidence level ($t_{0.05,1000}$) are also reported.

Q[a] ($l\,min^{-1}$)	θ[b] (°C)	w (mm)	B ...	S ...	$t_{0.05,1000}$ ...	Re_{2h} ...	Re_τ
257 ± 2.2	24.1 ± 0.29	800 ± 5	74	3.7	1.962	5882 ± 74.3 (±1.3%)	187 ± 2.1 (±1.1%)
560 ± 3.6	23.8 ± 0.29	800 ± 5	143	2.3	1.962	12 727 ± 143 (±1.1%)	368 ± 3.6 (±1%)
1217 ± 6.4	23.6 ± 0.29	800 ± 5	294	3.1	1.962	27 516 ± 294 (±1.1%)	726 ± 6.8 (±0.9%)

[a]Fixed error provided by the sensors manufacturer.
[b]Fixed error computed as the root-sum-square of the error originating from the PT100 sensor (±0.15 °C), the one introduced by the 300TX signal transmitter (±0.25 °C), and the calibration error produced by the Thermo Scientific AC200 circulator (±0.01 °C).

TABLE IV. Flow parameters and settings of the midspan experiments (Sec. III A).

Flow scales					
Re_τ			187	368	726
θ		(°C)	24.1	23.8	23.6
u_τ		(mm/s)	4.3	8.4	16.3
l_ν		(mm)	0.21	0.11	0.05
Settings of the PIV measurements					
Separation time		(ms)	4	2	1
Magnification				0.25	
Field of view		(mm^2)		65× 21	
		(Pixel)		1600× 512	
Tokina AT-X pro macro					
Objective	f	(mm)		100	
	$f_\#$			8	
	Material			Polyamide	
Tracers	Density	(g/cm^3)		1.03	
	Diameter	(μm)		20	
	Concentration	[ppp([a])]		0.03	

[a]ppp: particles per pixel.

flow meter, the shear velocity has to be inferred, and the control system relies on linking the shear Reynolds number (Re_τ) to the bulk Reynolds number (Re_{2h}) via an empirical correlation. To achieve this aim, we used the correlation (8) proposed by Pope,[74] which allows us to determine the shear velocity u_τ, as described extensively in Sec. II E. In this section, we quantify the accuracy of this correlation in the frame of our facility and compare the value of the shear Reynolds number predicted by the correlation (8) (Re_τ) against the shear Reynolds number measured from a physically grounded fitting procedure ($Re_{\tau,f}$). We consider the experimental measurements presented in Sec. III A, and we follow the procedure described in the following.

Extracting the shear velocity from the PIV measurements is enabled by fitting a theoretically motivated mean velocity profile to the measured one.[58,97–99] We used a composite model made up of an inner $\langle u^+_{inner}\rangle$ and an outer $\langle u^+_{outer}\rangle$ layer fitting.[98] The inner and outer layers overlap between $y^+ > 50$ and $y/h < 0.1$[74] for high Reynolds numbers ($Re_\tau = 10^4$). We use the standard notation in which length and velocity with "+" are made dimensionless with respect to the viscous length scale (l_ν) and shear velocity (u_τ), respectively. The chosen fittings consist of a linear behavior near the wall[100] ($y^+ < 11$),

$$u^+ = y^+, \tag{13}$$

the overshoot above the logarithmic profile[101] at $y^+ \approx 50$, the logarithmic profile[102]

$$u^+ = 1/\kappa \ln y^+ + \beta, \tag{14}$$

with κ and β constant coefficients, and the wake profile at the channel center.[103] The no-slip boundary condition has been considered by setting $u^+(y^+ = 0) = 0$. The location of the wall ($y^+ = 0$)[104] has been measured with pixel accuracy based on the laser sheet reflected from the channel bottom wall in the camera image. The symmetry of the flow across the center line has been accounted for in the wake function (see Nagib and Chauhan[98] for additional details).

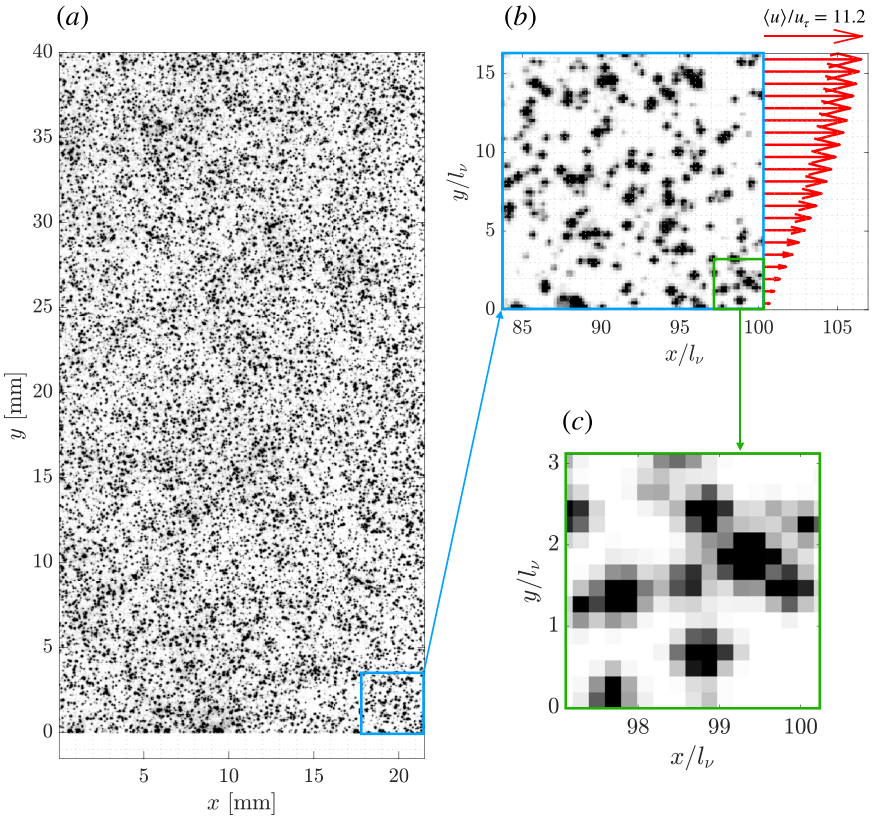

FIG. 5. Example of pre-processed image (grayscale inverted) for a wall-normal measurement obtained at $Re_\tau = 187$. (a) Entire field of view, with dimensions in mm. (b) Detail of the near-wall region (dimensions in wall-units), with corresponding time-averaged and horizontally averaged streamwise velocity profiles (red vectors). (c) Final interrogation window (green box).

The inner layer velocity profile $\langle u^+_{inner} \rangle$ has been computed by integrating Eq. (3) from Nagib and Chauhan,[98] where the parameter s has been found by matching the inner to the outer layer profiles at $y^+ = 150, 250,$ and 300 for $Re_\tau = 187, 368,$ and 726, respectively. The outer layer velocity profile $\langle u^+_{outer} \rangle$ was modeled by Eqs. (6) and (12) from Nagib and Chauhan.[98] The Kármán constant $\kappa = 0.37$, the intercept value $\beta = 3.7$, and the wake parameter $\Pi = 0.05$ have been used as they are considered the most probable for channel flow at high Reynolds numbers.[98] We wish to remark that the non-universality of these values has been observed,[47,98,99,104–111] and they were found to be dependent on flow geometry (e.g., channel, pipe, and boundary layer flows) and Reynolds number. Finally, the shear velocity is obtained by minimizing the mean squared difference between the composite profile and the measured profile $\langle u \rangle / u_\tau$ (a procedure similar to the one employed by Kendall and Kooches-fahani[97]) using the `fminbnd` function in MATLAB.[112] As an initial guess for u_τ, the correlation (8) proposed by Pope[74] has been used.

The velocity profiles used to determine the shear velocity are the ones reported in Sec. III A. Corresponding fitted profiles are shown in Fig. 14 in the Appendix. We obtain that the shear Reynolds numbers measured from the fitting of the profiles ($Re_{\tau,f}$) are in agreement with the predictions obtained via correlation (8) (Re_τ). In particular, we found $Re_{\tau,f} = 194, 374,$ and 737, corresponding to $Re_\tau = 187, 368,$ and 726, respectively. The relative difference between the value measured by fitting and the value predicted by the correlation is shown in Fig. 9. The discrepancy is lower than 3.5%, and the larger Re_τ, the lower the difference observed, reducing to 1.4% in the instance of $Re_\tau = 726$. The accuracy of this correlation diminishes at larger Reynolds numbers ($Re_\tau > 3000$), and alternative strategies should be used, as discussed in Sec. II E.

C. Measurements at different span-wise locations

Direct numerical simulations are classically performed in span-wise periodic domains (channels), whereas experimental measurements are limited to duct flows having a finite span. To enable a comparison between experimental ducts and numerical channels, the influence of the sidewalls needs to be quantified. Vinuesa, Schlatter, and Nagib[49] investigated numerically the flow in a duct of aspect ratio $\mathcal{AR}$ at $Re_\tau = 180$. They observed that the influence of secondary motions induced by the presence of the side-walls extends up to $\approx 5h$ away from the side-walls, being h the half-channel height. To provide experimental evidence of these findings, we performed PIV experiments at $Re_\tau = 180$ at four span-wise locations. We measured first and second order moments of the stream-wise velocity, and we compared our findings with the numerical results of channel and duct flows.

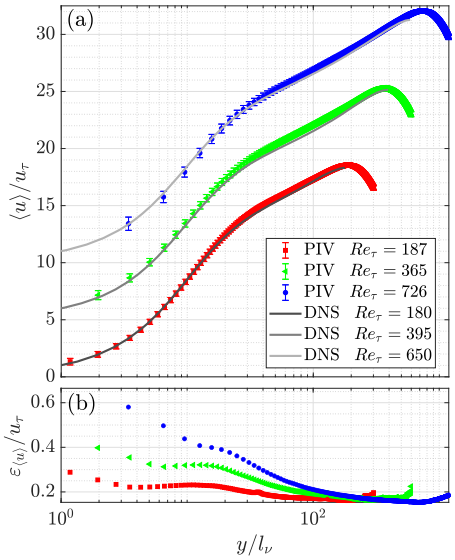

FIG. 6. (a) Dimensionless profiles of the streamwise mean velocities. For better readability, profiles are shifted upward by $5\langle u \rangle / u_\tau$. The uncertainties of the streamwise mean velocities normalized by the slip velocity (ε/u_τ) are shown in panel (a) as error bars and more in detail in panel (b).

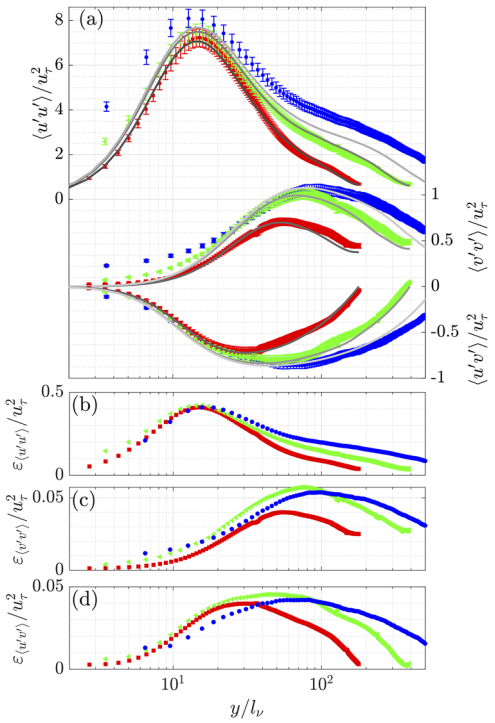

FIG. 7. (a) Dimensionless profiles of the Reynolds stresses. Left axis: streamwise component. Right axis: span-wise and shear component. The normalized uncertainties of the Reynolds-stresses (ε/u_τ^2) are shown in panel (a) as error bars and more in detail in panels (b)–(d). Legend is the same as in Fig. 6.

The geometry and flow configuration considered in the experiments match the setup used in the numerical simulations (i.e., same $\mathcal{AR}$ and Re_τ). The experimental measurements have been recorded at four spanwise locations, namely $z/h = 0, 5, 7.5$ and 9.25, from midspan to near side-walls, respectively. The measurements consist of 5000 image pairs separated by 1 s. The time separation (Δt) between the frames of each pair has been set to have a displacement of ≈11 px at the channel center ($y = h$), corresponding to Δt between 7 ms (spanwise centerline) and 10 ms (near the side-walls). The optical magnification was 0.18, with a final interrogation window size of 24 × 24 px to capture 6 to 8 seeding particles within, with 75% overlap. We refer to Table IV for additional experimental details.

The results of the PIV measurements are compared in Fig. 10 against the DNS of duct flow,[49] and we find agreement between our measurements and the numerical results at all four span-wise locations considered. The uncertainties of these measurements are comparable to those shown in Sec. III A in Figs. 6(b) and 7(b). We analyze the evolution of the flow with respect to the midspan measurements ($z/h = 0$). Note that the mean velocity in Fig. 10(a) is scaled with respect to the centerline mid-span velocity (u_c), and the Reynolds stresses in Fig. 10(b) are normalized with their maximum value at the midspan, $u'u'_{\max}$. The mean velocity and Reynolds stresses at $z/h = 5$ deviate within 2% and 5% from the midspan measurements, respectively. This difference is in agreement with the numerical findings, suggesting that first and second order statistics, at this Reynolds number and this aspect ratio, are not significantly affected by secondary motions within a distance of $z = 5h$ from the midspan. In addition, a comparison with channel simulations[80] ($\mathcal{AR} = \infty$) is presented in Fig. 10(a). In addition, in this case, no significant difference is observed between experiments and simulations. For $z/h = 7.5$, we find deviations from the midspan profiles within 14% and 25% for the mean velocity and Reynolds stresses, respectively. This result is still consistent with the numerical simulations and shows that at this location, the effect of the sidewalls is already remarkable. Approaching the side walls ($z/h = 9.25$), measurements indicate a large deviation from the mid-span profiles: the mean velocity and Reynolds stresses deviate from the midspan reference by 25% and 80%, respectively. Finally, we compare in the inset of Fig. 10(a) the centerline velocity (i.e., at $y = h$) along the span-wise direction z, and we also observe in this case a good agreement with the duct simulations. These results confirm previous numerical findings[49] and suggest that, for $\mathcal{AR} = 10$ and $Re_\tau = 180$, first and second order statistics computed within the region $-5 \le z/h \le 5$ are representative of a channel flow configuration,[80] i.e., with negligible influence from the side walls, corresponding to a difference ≤5% with respect to the midspan measurements.

IV. APPLICATION: FIBER TRACKING IN TURBULENT FLOWS

An example of a particle measurement in turbulent channel flow is provided in this section. As a dispersed phase, we used fibers, which are slender particles that are small compared to the channel size (≈1/100) and of the same order as the smallest flow structures (Kolmogorov length scale at the wall). The aim is twofold: (i) performing measurements of fiber trajectory and orientation that span over a region of the channel that is much larger compared to

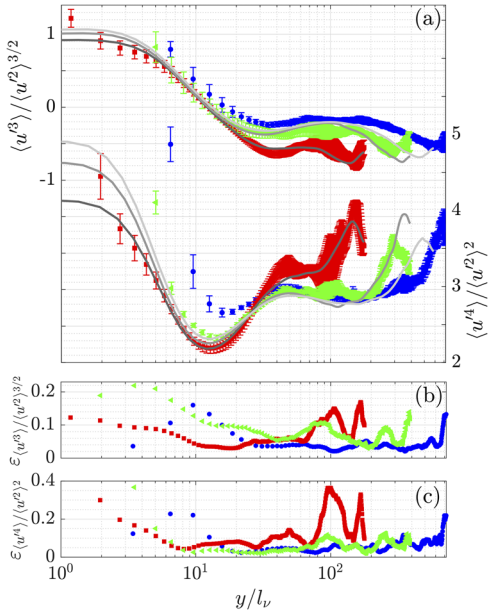

FIG. 8. (a) Dimensionless profiles of skewness (top, left axis) and flatness (bottom, right axis) for the streamwise velocity component. The normalized uncertainties of skewness and flatness (ε) are shown in panel (a) as error bars and more in detail in panels (b) and (c). Legend is the same as in Fig. 6.

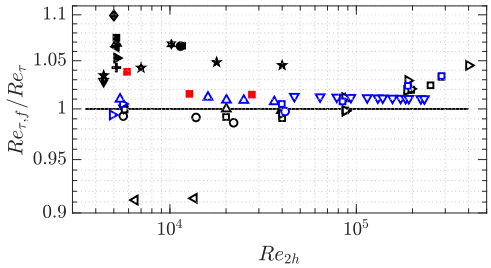

FIG. 9. Comparison of the shear Reynolds number measured by the fitting procedure ($Re_{\tau,f}$) and predicted by the correlation (8) (Re_τ) as a function of the bulk Reynolds number (Re_{2h}). The deviation of experimental measurements presented in Sec. III A (red symbols) with respect to the correlation (8) proposed by Pope[74] (solid line) is reported, together with numerical (filled symbols) and experimental (open symbols) literature results (legend as in Fig. 4). The shear Reynolds number measured by fitting differs by 3.5%, 1.5%, and 1.4% from the prediction of the correlation for the three experiments considered.

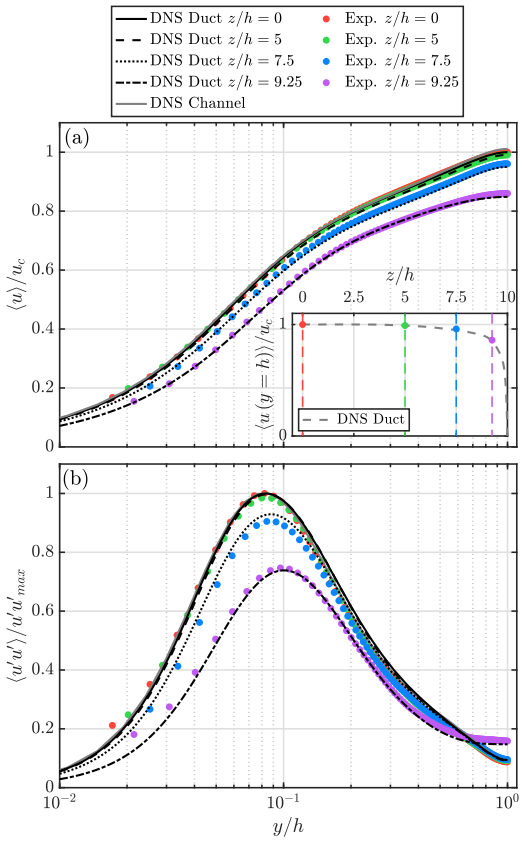

FIG. 10. Wall-normal statistics of stream-wise velocity (u) at different span-wise locations for $Re_\tau = 180$. Experiments (symbols, present facility, $\mathcal{AR} = 10$), duct simulation[49] (black lines, $\mathcal{AR} = 10$), and channel simulation[80] (gray line, $\mathcal{AR} = \infty$) are compared. (a) Mean velocity scaled by the centerline mid-span velocity u_c, with $u_c = \langle u\rangle|_{y=h,z=0}$. In the inset, the centerline velocity along the spanwise direction is reported. (b) Reynolds stresses scaled by the mid-span peak value, $u'u'_{max}$.

the fibers' size; and (ii) determining the orientation and rotation of millimeter-scale anisotropic objects. After acquisition with the high-speed system described in Sec. II C, images are processed to identify, track, and determine the orientation of each fiber. In the following, we report the length scales involved (Sec. IV A), the reconstruction method (Sec. IV B), and finally, the influence of the number of cameras on the measurement performed (Sec. IV C).

A. Fiber properties

The fibers used are Polyamide 6.6 Precision Cut Flock (Flockan), which has a linear density of 9×10^{-8} kg/m (0.9 dtex). The density and cutting length are 1150 kg/m^3 and $L_f = 1.2$ mm, respectively, corresponding to a diameter $d \approx 10$ μm. We consider one flow condition corresponding to $Re_\tau = 726$.

Fiber shape varies, as visible in Fig. 11(a), where a picture of dry fibers is shown. This represents both an issue because complex geometry makes the reconstruction more challenging and an advantage since the orientation of these anisotropic shaped objects can be uniquely determined. The distribution of fibers' length, L_f, is clearly centered at the nominal length (additional details provided by Alipour, De Paoli, and Soldati[41]), which is small compared to the channel height (80 mm). At the same time, L_f is comparable to the smallest scales of the flow, indicated as the Kolmogorov length scale (η), which is minimum at the wall ($\eta \approx 0.08$ mm) and maximum at the center ($\eta \approx 0.28$ mm), and we have that the relative length of the fibers with respect to the Kolmogorov length scales is in the range

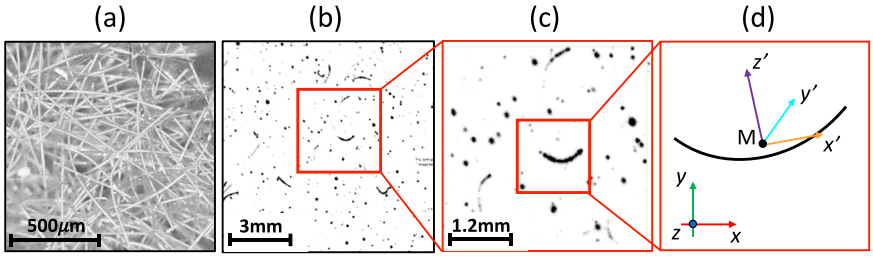

FIG. 11. (a) Microscope image of dry fibers. (b) Pre-processed image of tracers and fibers from one camera (only a small region is shown). (c) Close up view of a fiber. Note that the view of the camera is not perpendicular with respect to the orientation of the illumination volume; therefore, the scale reported in (b) and (c) is approximate. (d) Sketch of a reconstructed fiber with an indication of the reference frame of the laboratory (x, y, z, fixed) and the reference frame of the fiber (x', y', z', moving with the fiber) centered at the center of mass, M.

$4 \leq L_f/\eta \leq 15$, from the center of the channel to the wall. Note that in this facility and at lower shear Reynolds numbers, fibers' length can be the same size as the local Kolmogorov length scale in the center; e.g., for $Re_\tau \approx 180$, at $y = h$, the relative fiber size is $L_f/\eta \approx 1.6$.

Fibers are initially dispersed in the downstream reservoir and flow through the pump to the upstream reservoir and finally to the channel. The concentration of fibers employed is very low (volume fraction $\leq 10^{-6}$), so the effect of the fibers on the flow as well as the fiber–fiber interactions can be neglected[1] (one-way coupling). In addition to the fibers, the flow is seeded with tracers (diameter of 20 μm) for calibration purposes, and it is finally recorded in the test section. An example of a recorded image is reported in Fig. 11(b), where both tracers (circular objects) and fibers (elongated objects) are visible. The subsequent reconstruction required to determine fiber orientation and position is described in Sec. IV B.

B. Fiber tracking technique

When the flow evolution is recorded by two or more cameras, the collected images can be used to infer the position and orientation of the fibers in three-dimensional physical space. The method used here is a combination of commercial and in-house codes, which is described in detail by Alipour *et al.*[40] We provide here a summary of the algorithm, which consists of the following four main steps:

1. *MART reconstruction.*
   For each time-step, one image per camera is acquired and pre-processed (spatial and time filtering) using DaVis 10.2.1 (LaVision GmbH). The three-dimensional light intensity distribution is reconstructed from the images using the Multiplicative Algebraic Reconstruction Technique[65] (MART).
2. *Phase discrimination.*
   Each voxel contained in the obtained three-dimensional object corresponds to either a fiber, a tracer, an optical disturbance, or a numerical artifact due to MART. Therefore, discrimination based on the light intensity and shape of connected regions is employed to identify each voxel belonging to the fibers. The remaining voxels are discarded. This step is achieved with in-house MATLAB code.
3. *Fiber modeling.*
   For the flow conditions and the fiber properties considered, fibers do not deform significantly due to the action of the fluid (deformation estimated to be <1%[41]), so their shape does not change over time. We observed that the fibers' shape is well approximated by a second order polynomial.[40] For each cluster of voxels in each time-step, the best-fitting second-order polynomial (in a least-squares sense) is determined and used to find the fiber reference frame (x', y', z') in Fig. 11(d).
4. *Determination of fiber position and orientation.*
   Finally, each fiber is tracked by searching for its center of mass within a chosen radius in two consecutive snapshots. The temporal evolution of position and orientation of the fiber reference frame (x', y', z') with respect to the laboratory reference frame (x, y, z) is used to compute the translation velocity and rotation rate of each fiber.

This measurement procedure can be applied to different camera configurations. In Sec. IV C, we will present the results relative to the camera configuration labeled *span-wise* in Sec. II C.

C. Effect of numbers of cameras on fiber reconstruction

Cameras represent key components of the apparatus and, in particular, of the measurement system. In the context of multiphase flows, the shape and position of the objects are not known *a priori*, so a limited number of cameras could be a drawback and affect the uncertainty of the reconstruction.[113] In addition, complex dynamics has to be recorded at a high frame rate for multiphase flows of practical interest, making high-speed cameras critical components in the budget of an experimental setup. Therefore, determining the required number of cameras is crucial, as it influences the accuracy of the measurements and the cost of the facility. In this section, we will analyze the effect of the number of cameras on the fibers' reconstruction performed in the TU Wien Turbulent Water Channel, leading to the use of a certain number of cameras.

The influence of the number of cameras on the quality of tomographic reconstruction has been previously investigated.[53,57,59–61,65] Elsinga *et al.*[65] used synthetically generated particles to investigate the effect of the number of cameras on the reconstruction quality, defined as the normalized correlation coefficient between the generated intensity distribution and the reconstructed one. They found that increasing the number of cameras correlated with higher reconstruction quality. This effect is more pronounced for measurements performed with a high number of particles per pixel. In this work,

TABLE V. Specifications of the six camera setup.

Parameter	Value
Calibration target	LaVision 058–5
Calibration model	Third order polynomial
Scale factor	41.7 px mm^{-1}
Geometrical calibration fit error	<0.73px
Measurement domain ($x \times y \times z$)	$40 \times 34 \times 15$ mm^3
Number of subdomains ($x \times y \times z$)	$15 \times 13 \times 10$
Calibration average disparity after VSC	0.01 voxel
Calibration maximum disparity after VSC	0.23 voxel
Min. angle between two cameras	15.46°
Max. angle between two cameras	55.42°

we propose a similar analysis and provide qualitative and quantitative indications of the effect of the number of cameras on the quality of fiber reconstruction.

We performed a fiber tracking experiment at $Re_\tau = 726$, and we reconstructed the fibers using 6, 5, 4, and 3 cameras. MART (see Sec. IV B) has been repeated by discarding 1, 2, and 3 cameras for the 5, 4, and 3 camera configurations, respectively. The experiment was performed in the *span-wise* camera configuration shown in Fig. 2(c), in which the reconstructed volume is a wall-parallel slice located at the upper region of the channel and having a thickness of 272 wall units. Camera setup parameters are summarized in Table V. The Volume-Self-Calibration[114] (VSC) achieved with six cameras has been used in all cases. We collected 3000 frames separated by a time of 1.25 ms. In each frame, ≈40 fibers were visible. This is equivalent to a volume fraction of $\approx 2 \times 10^{-7}$. We processed ≈2000 tracks longer than ten time-steps.

A qualitative comparison of the 3D light intensity distribution of one fiber reconstructed with 6, 5, 4, and 3 cameras is provided in Figs. 12(a)–12(d), respectively. The second order fitted polynomial is shown as a black line, and the fiber co-moving coordinate system is shown as red, green, and blue vectors. We observe that decreasing the number of cameras used corresponds to an increase in the noise of the reconstructed light intensity field. This affects the fitted polynomial, as seen most clearly by comparing Figs. 12(a) and 12(d). The curvature measurement is consistent for the 6, 5, and 4 camera reconstructions but fails when using only 3 cameras. A second observable effect is the higher spread of the light intensity when using only three cameras, which results in higher fiber length estimations.

To quantify the reconstruction quality for different numbers of cameras, we exploit the non-deformability (for details, see Sec. IV B) of the fibers by comparing the fiber shape reconstructions in each time-step with the track average in terms of length and curvature fluctuations. We define the fiber length fluctuations as $L'_f = |L_{i,k} - \langle L_{i,k}\rangle_i|$, where $L_{i,k}$ is the length of the fiber of track i at time-step k. Similarly, we define the absolute curvature fluctuations $\kappa' = |\kappa_{i,k} - \langle \kappa_{i,k}\rangle_i|$, where $\kappa_{i,k}$ is the fiber curvature of track i at time-step k. The track-average of track i is denoted by $\langle\cdot\rangle_i$, and by $|\cdot|$, the absolute value is meant. Low values of both quantities signify low temporal deviations of fiber reconstructed shapes from the average shape. Probability density function (pdf) estimates of the fiber length and curvature fluctuations are reported in Figs. 13(a) and 13(b),

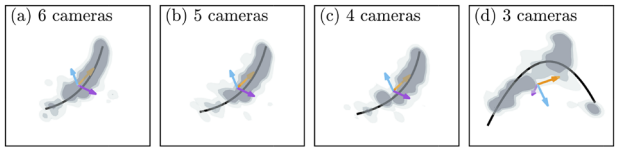

FIG. 12. Fiber light intensity reconstructed with 6, 5, 4, and 3 cameras is shown in (a)–(e), respectively. The black lines represent the second order polynomial fit. The fiber reference frame (x', y', z') is shown by the orange, cyan, and purple vectors. Three iso-surfaces of light intensity normalized by the maximum are shown: 0.2, 0.4, and 0.6. Darker colors represent higher light intensity. Transparency has been used for visualization purposes.

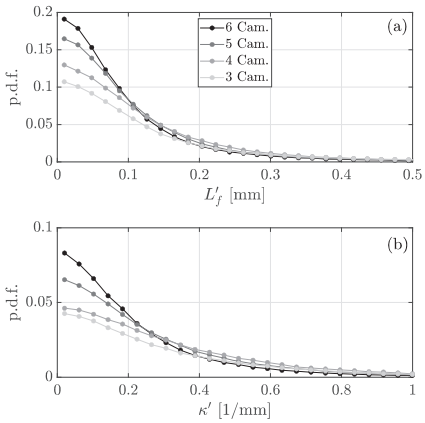

FIG. 13. Probability density function (pdf) estimates of fiber length (L'_f) and curvature (κ') fluctuations are shown in panels (a) and (b), respectively. Both parameters are defined in Sec. IV C. Bin sizes are 0.02 mm and 0.04 mm^{-1} for panels (a) and (b), respectively. The legend is valid for both panels.

respectively. The peak of the fiber length fluctuations pdf [Fig. 13(a)] of the six camera configurations was higher by 16%, 47%, and 78% than the 5, 4, and 3 camera configurations, respectively. The fiber curvature fluctuations pdf [Fig. 13(b)] show the peak for 6 camera reconstruction higher by 27%, 80%, and 95% than the 5, 4, and 3 camera setups, respectively.

Overall, we observed that increasing the number of cameras from 3 to 6 increases the likelihood that a reconstructed fiber shape is close to the track-averaged shape. This implies that the tomographic reconstruction quality increases with the number of cameras used, which is consistent with the findings of Elsinga *et al.*[65] The improvement in results observed by increasing the number of cameras is obtained for a significant database, but it is relative to this specific configuration. For instance, using a different camera exclusion order might result in different quantitative results. A number of additional factors (e.g., particle image concentration, fiber concentration, magnification, and viewing angle) may also affect the quality of the reconstruction, and we leave the study of these effects for future work.

V. SUMMARY AND OUTLOOK

A new experimental facility, the TU Wien Turbulent Water Channel, has been built. It has shear Reynolds number control

and allows studying the dynamics of anisotropic particles in wall-bounded turbulence. The channel is made of Plexiglas, and it recirculates 3000 l of water. The measurement section is 8.5 m away from the inlet and has an internal height of 0.08 m and a width of 0.8 m. The facility produces shear Reynolds numbers of up to 1580 controlled within ±0.1% for repeatable and consistent hour-long experiments. The transparent design allows for multiple camera and illumination arrangements, enabling techniques such as Particle Image Velocimetry and Particle Tracking Velocimetry. Measurements of the turbulent flow and anisotropic particles such as microplastic fibers are made possible. The dynamics of curved fibers in turbulent channel flows has not been investigated yet, and an accurate definition of the relevant fibers' dimensionless parameters is not available. Therefore, the channel has been specifically designed to perform experiments with real-size microplastics (1–5 mm in length), with the particles being much smaller than the channel height (80 mm). The agreement of single-phase measurements at the mid-span of the duct with numerical periodic channels confirms the geometry-independence of statistical quantities such as mean stream-wise velocity, Reynolds stresses, skewness, and flatness. This is also supported by the observed deviations from the mid-span profiles within 2% and 5% of the mean stream-wise velocity and Reynolds stresses, respectively, at 20 cm away from the mid-span.

Finally, we describe the procedure used to measure the shape, position, and orientation of microplastic fibers in a turbulent channel flow. An example of a fiber reconstruction is given, and we found that increasing the number of cameras from 3 to 6 improves the reconstruction quality significantly.

For the future, we reserve studying particle interaction with open-channel turbulent flows. This will require extending the system controlling the pressure head.

SUPPLEMENTARY MATERIAL

See the supplementary material for the experimental profiles obtained in the present study and shown in Figs. 6–8 and 10.

ACKNOWLEDGMENTS

The authors acknowledge Mr. Franz Neuwirth and Mr. Werner Jandl for their help with the design and construction of the experimental facility. The authors acknowledge the students Silvia Sambuca, Kylian Keiml, and Koray Aldik for their assistance. Professor Sina Ghaemi is acknowledged for many useful discussions.

The authors acknowledge the TU Wien University Library for financial support through its Open Access Funding Program. V.G. acknowledges the financial support provided by FSE S3 HEaD (Grant No. 1619942002). A.S. acknowledges the generous endowment funding from TU Wien. This research was funded in part by the Austrian Science Fund (FWF) (Grant No. P-35505). V.G. and A.S. also gratefully acknowledge funding from the PRIN project "Advanced computations and experiments in turbulent multiphase flow" (Project No. 2017RSH3JY).

AUTHOR DECLARATIONS

Conflict of Interest

The authors have no conflicts to disclose.

Author Contributions

Vlad Giurgiu: Conceptualization (equal); Data curation (equal); Formal analysis (lead); Investigation (equal); Methodology (supporting); Software (lead); Validation (lead); Visualization (lead); Writing – original draft (equal); Writing – review & editing (equal). **Giuseppe Carlo Alp Caridi**: Conceptualization (equal); Formal analysis (equal); Investigation (equal); Project administration (equal); Software (supporting); Supervision (lead); Validation (supporting); Visualization (equal); Writing – original draft (supporting). **Mobin Alipour**: Conceptualization (equal); Funding acquisition (equal); Methodology (equal); Software (supporting). **Marco De Paoli**: Conceptualization (equal); Data curation (equal); Formal analysis (equal); Funding acquisition (equal); Investigation (equal); Methodology (equal); Project administration (equal); Software (equal); Supervision (equal); Validation (supporting); Visualization (equal); Writing – original draft (equal); Writing – review & editing (lead). **Alfredo Soldati**: Conceptualization (equal); Funding acquisition (equal); Project administration (equal); Resources (equal); Supervision (equal); Writing – review & editing (equal).

DATA AVAILABILITY

The data that support the findings of this study are available within the article and its supplementary material.

APPENDIX: MEAN PROFILES USED FOR SHEAR VELOCITY MEASUREMENTS

Measurements of the shear velocity are obtained by fitting the profiles to the measured mean stream-wise velocity profiles, as discussed in Sec. III B. Three different shear Reynolds numbers are considered, and the profiles are shown in Fig. 14. The experimental

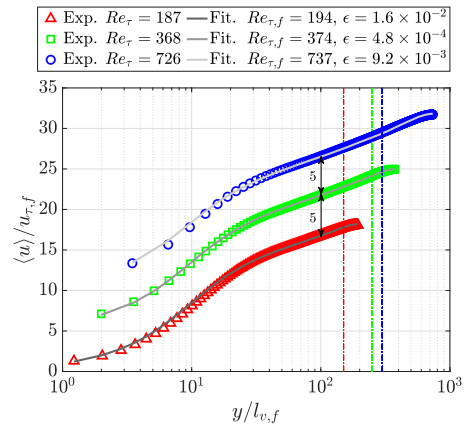

FIG. 14. Stream-wise velocity profiles presented in Sec. III A (Exp., symbols) and obtained from composite fittings as described in Sec. III B (Fit., lines) are shown as a function of y. The wall-normal coordinate is scaled here by the viscous length scale resulting from the fitting shear Reynolds number (subscript f). The mean squared difference between the fitted and measured profiles, scaled by the shear velocity found by fitting, is denoted by ε. Vertical dashed–dotted lines indicate the wall-normal locations where the outer and inner profiles have been connected. The profiles have been shifted by the value indicated next to the double black arrows for clarity.

velocity profiles are the same as the ones reported in Sec. III A. Following the fitting procedure discussed in Sec. III B, the fitted values of shear velocity are determined. We found the difference between the fitted ($Re_{\tau,f}$) and the predicted (Re_τ) shear Reynolds numbers to be as high as 3.5%, 1.5%, and 1.4% for the lowest, medium, and highest shear Reynolds numbers, respectively. This implies that given the bulk Reynolds number, the correlation (8) provides a good estimate for the shear Reynolds number; nonetheless, it can be improved, and we leave this as a possible future development.

REFERENCES

[1] L. Brandt and F. Coletti, "Particle-laden turbulence: Progress and perspectives," Annu. Rev. Fluid Mech. **54**, 159–189 (2022).
[2] H. A. Leslie, M. J. M. van Velzen, S. H. Brandsma, A. D. Vethaak, J. J. Garcia-Vallejo, and M. H. Lamoree, "Discovery and quantification of plastic particle pollution in human blood," Environ. Int. **163**, 107199 (2022).
[3] L. K. Clark, M. H. DiBenedetto, N. T. Ouellette, and J. R. Koseff, "Dispersion of finite-size, non-spherical particles by waves and currents," J. Fluid Mech. **954**, A3 (2023).
[4] I. Chubarenko, A. Bagaev, M. Zobkov, and E. Esiukova, "On some physical and dynamical properties of microplastic particles in marine environment," Mar. Pollut. Bull. **108**, 105–112 (2016).
[5] G. A. Voth and A. Soldati, "Anisotropic particles in turbulence," Annu. Rev. Fluid Mech. **49**, 249–276 (2017).
[6] K. Senathirajah, S. Attwood, G. Bhagwat, M. Carbery, S. Wilson, and T. Palanisami, "Estimation of the mass of microplastics ingested—A pivotal first step towards human health risk assessment," J. Hazard. Mater. **404**, 124004 (2021).
[7] S. M. Abel, S. Primpke, I. Int-Veen, A. Brandt, and G. Gerdts, "Systematic identification of microplastics in abyssal and hadal sediments of the Kuril Kamchatka trench," Environ. Pollut. **269**, 116095 (2021).
[8] I. E. Napper, B. F. R. Davies, H. Clifford, S. Elvin, H. J. Koldewey, P. A. Mayewski, K. R. Miner, M. Potocki, A. C. Elmore, A. P. Gajurel, and R. C. Thompson, "Reaching new heights in plastic pollution—Preliminary findings of microplastics on Mount Everest," One Earth **3**, 621–630 (2020).
[9] P. S. Ross, S. Chastain, E. Vassilenko, A. Etemadifar, S. Zimmermann, S.-A. Quesnel, J. Eert, E. Solomon, S. Patankar, A. M. Posacka, and B. Williams, "Pervasive distribution of polyester fibres in the Arctic Ocean is driven by Atlantic inputs," Nat. Commun. **12**, 106–109 (2021).
[10] K. Ugwu, A. Herrera, and M. Gómez, "Microplastics in marine biota: A review," Mar. Pollut. Bull. **169**, 112540 (2021).
[11] E. S. Gruber, V. Stadlbauer, V. Pichler, K. Resch-Fauster, A. Todorovic, T. C. Meisel, S. Trawoeger, O. Hollóczki, S. D. Turner, W. Wadsak *et al.*, "To waste or not to waste: Questioning potential health risks of micro- and nanoplastics with a focus on their ingestion and potential carcinogenicity," Exposure Health **15**, 33–51 (2022).
[12] M. Kooi and A. Koelmans, "Simplifying microplastic via continuous probability distributions for size, shape, and density," Environ. Sci. Technol. Lett. **6**, 551–557 (2019).
[13] H. Brenner, "The Stokes resistance of an arbitrary particle—IV arbitrary fields of flow," Chem. Eng. Sci. **19**, 703–727 (1964).
[14] N. Challabotla, L. Zhao, and H. Andersson, "Orientation and rotation of inertial disk particles in wall turbulence," J. Fluid Mech. **766**, R2 (2015).
[15] C. Marchioli and A. Soldati, "Rotation statistics of fibers in wall shear turbulence," Acta Mech. **224**, 2311–2329 (2013).
[16] C. Marchioli, L. Zhao, and H. I. Andersson, "On the relative rotational motion between rigid fibers and fluid in turbulent channel flow," Phys. Fluids **28**, 013301 (2016).
[17] R. Mallier and M. Maxey, "The settling of nonspherical particles in a cellular flow field," Phys. Fluids A **3**, 1481–1494 (1991).
[18] H. Shin and M. Maxey, "Chaotic motion of nonspherical particles settling in a cellular flow field," Phys. Rev. E **56**, 5431 (1997).
[19] A. Abbasi Hoseini, F. Lundell, and H. I. Andersson, "Finite-length effects on dynamical behavior of rod-like particles in wall-bounded turbulent flow," Int. J. Multiphase Flow **76**, 13–21 (2015).
[20] K. M. O. Håkansson, M. Kvick, F. Lundell, L. Prahl Wittberg, and L. D. Söderberg, "Measurement of width and intensity of particle streaks in turbulent flows," Exp. Fluids **54**, 1555–1613 (2013).
[21] J. S. Paschkewitz, C. D. Dimitropoulos, Y. X. Hou, V. S. R. Somandepalli, M. G. Mungal, E. S. G. Shaqfeh, and P. Moin, "An experimental and numerical investigation of drag reduction in a turbulent boundary layer using a rigid rodlike polymer," Phys. Fluids **17**, 085101 (2005).
[22] L. J. Baker and F. Coletti, "Particle–fluid–wall interaction of inertial spherical particles in a turbulent boundary layer," J. Fluid Mech. **908**, A39 (2021).
[23] L. J. Baker and F. Coletti, "Experimental investigation of inertial fibres and disks in a turbulent boundary layer," J. Fluid Mech. **943**, A27 (2022).
[24] Y. Ninto and M. H. Garcia, "Experiments on particle—Turbulence interactions in the near–wall region of an open channel flow: Implications for sediment transport," J. Fluid Mech. **326**, 285–319 (1996).
[25] S. So, H. Morikita, S. Takagi, and Y. Matsumoto, "Laser Doppler velocimetry measurement of turbulent bubbly channel flow," Exp. Fluids **33**, 135–142 (2002).
[26] Y. Suzuki, M. Ikenoya, and N. Kasagi, "Simultaneous measurement of fluid and dispersed phases in a particle-laden turbulent channel flow with the aid of 3-D PTV," Exp. Fluids **29**, S185–S193 (2000).
[27] S. Zade, W. Fornari, F. Lundell, and L. Brandt, "Buoyant finite-size particles in turbulent duct flow," Phys. Rev. Fluids **4**, 024303 (2019).
[28] W. Abu Rowin and S. Ghaemi, "Streamwise and spanwise slip over a superhydrophobic surface," J. Fluid Mech. **870**, 1127–1157 (2019).
[29] W. Abu Rowin and S. Ghaemi, "Effect of Reynolds number on turbulent channel flow over a superhydrophobic surface," Phys. Fluids **32**, 075105 (2020).
[30] R. van Hout, "Time-resolved PIV measurements of the interaction of polystyrene beads with near-wall-coherent structures in a turbulent channel flow," Int. J. Multiphase Flow **37**, 346–357 (2011).
[31] S. Kuperman, L. Sabban, and R. van Hout, "Inertial effects on the dynamics of rigid heavy fibers in isotropic turbulence," Phys. Rev. Fluids **4**, 064301 (2019).
[32] S. Shaik and R. van Hout, "Kinematics of rigid fibers in a turbulent channel flow," Int. J. Multiphase Flow **158**, 104262 (2023).
[33] A. Capone, M. Miozzi, and G. P. Romano, "On translational and rotational relative velocities of fibers and fluid in a turbulent channel flow with a backward-facing step," Int. J. Multiphase Flow **94**, 189–200 (2017).
[34] A. Capone, F. Di Felice, and F. Alves Pereira, "Flow-particle coupling in a channel flow laden with elongated particles: The role of aspect ratio," J. Mar. Sci. Eng. **9**, 1388 (2021).
[35] Y. Murai, Y. Oishi, Y. Takeda, and F. Yamamoto, "Turbulent shear stress profiles in a bubbly channel flow assessed by particle tracking velocimetry," Exp. Fluids **41**, 343–352 (2006).
[36] K. T. Kiger and C. Pan, "Suspension and turbulence modification effects of solid particulates on a horizontal turbulent channel flow," J. Turbul. **3**, 019 (2002).
[37] A. Kitagawa, K. Hishida, and Y. Kodama, "Flow structure of microbubble-laden turbulent channel flow measured by PIV combined with the shadow image technique," Exp. Fluids **38**, 466–475 (2005).
[38] B. Gvozdić, O. Dung, D. van Gils, G. Bruggert, E. Alméras, C. Sun, D. Lohse, and S. Huisman, "Twente mass and heat transfer water tunnel: Temperature controlled turbulent multiphase channel flow with heat and mass transfer," Rev. Sci. Instrum. **90**, 075117 (2019).
[39] O.-Y. Dung, P. Waasdorp, C. Sun, D. Lohse, and S. G. Huisman, "The emergence of bubble-induced scaling in thermal spectra in turbulence," J. Fluid Mech. **958**, A5 (2023).
[40] M. Alipour, M. De Paoli, S. Ghaemi, and A. Soldati, "Long non-axisymmetric fibres in turbulent channel flow," J. Fluid Mech. **916**, A3 (2021).
[41] M. Alipour, M. De Paoli, and A. Soldati, "Influence of Reynolds number on the dynamics of rigid, slender and non-axisymmetric fibres in channel flow turbulence," J. Fluid Mech. **934**, A18 (2022).
[42] J. Kim, "Progress in pipe and channel flow turbulence, 1961–2011," J. Turbul. **13**, N45 (2012).
[43] Y. Yamamoto and Y. Tsuji, "Numerical evidence of logarithmic regions in channel flow at $Re_\tau = 8000$," Phys. Rev. Fluids **3**, 012602 (2018).

[44]S. S. Dearing, M. Campolo, A. Capone, and A. Soldati, "Phase discrimination and object fitting to measure fibers distribution and orientation in turbulent pipe flows," Exp. Fluids **54**, 1419–1514 (2013).
[45]P. Bradshaw and G. Hellens, *The NPL 59 in. × 9 in. Boundary-Layer Tunnel* (Aeronautical Research Council, 1964).
[46]R. B. Dean, "Reynolds number dependence of skin friction and other bulk flow variables in two-dimensional rectangular duct flow," J. Fluids Eng. **100**, 215 (1978).
[47]E.-S. Zanoun, F. Durst, and H. Nagib, "Evaluating the law of the wall in two-dimensional fully developed turbulent channel flows," Phys. Fluids **15**, 3079–3089 (2003).
[48]R. Vinuesa, P. Schlatter, and H. M. Nagib, "On minimum aspect ratio for duct flow facilities and the role of side walls in generating secondary flows," J. Turbul. **16**, 588–606 (2015).
[49]R. Vinuesa, P. Schlatter, and H. M. Nagib, "Secondary flow in turbulent ducts with increasing aspect ratio," Phys. Rev. Fluids **3**, 054606 (2018).
[50]J. Laufer, "Investigation of turbulent flow in a two-dimensional channel," Ph.D. thesis, California Institute of Technology, 1948.
[51]K. Lien, J. Monty, M. Chong, and A. Ooi, "The entrance length for fully developed turbulent channel flow," in *15th Australian Fluid Mechanics Conference* (University of Sydney, Sydney, Australia, 2004), Vol. 15, pp. 356–363.
[52]J. Doherty, P. Ngan, J. Monty, and M. Chong, "The development of turbulent pipe flow," in 16th Australasian Fluid Mechanics Conference, 2007.
[53]F. Scarano, "Tomographic PIV: Principles and practice," Meas. Sci. Technol. **24**, 012001 (2012).
[54]S. Rafati and S. Ghaemi, "Evaluation of high magnification two and three dimensional particle image tracking/velocimetry in near wall turbulence," in 18th International Symposium on Applications of Laser and Imaging Techniques to Fluid Mechanics, Lisbon, Portugal, 2016.
[55]Q. Ye, F. F. J. Schrijer, and F. Scarano, "Geometry effect of isolated roughness on boundary layer transition investigated by tomographic PIV," Int. J. Heat Fluid Flow **61**, 31–44 (2016).
[56]D. R. Sabatino and T. Rossmann, "Tomographic PIV measurements of a regenerating hairpin vortex," Exp. Fluids **57**, 6–13 (2016).
[57]L. Thomas, B. Tremblais, and L. David, "Optimization of the volume reconstruction for classical Tomo-PIV algorithms (MART, BIMART and SMART): Synthetic and experimental studies," Meas. Sci. Technol. **25**, 035303 (2014).
[58]H. Mamori, K. Yamaguchi, M. Sasamori, K. Iwamoto, and A. Murata, "Dual-plane stereoscopic PIV measurement of vortical structure in turbulent channel flow on sinusoidal riblet surface," Eur. J. Mech. B/Fluids **74**, 99–110 (2019).
[59]K. P. Lynch and F. Scarano, "Experimental determination of tomographic PIV accuracy by a 12-camera system," Meas. Sci. Technol. **25**, 084003 (2014).
[60]Y. Fukuchi, "Influence of number of cameras and preprocessing for thick volume tomographic PIV," in Proceedings of 16th International Symposium on Applications of Laser Techniques to Fluid Mechanics, Lisbon, Portugal, 9–12 July 2012.
[61]F. J. W. de Almeida Martins, "Characterization of near-wall turbulent flows by tomographic PIV," Ph.D. thesis, Ecole Centrale de Lille; Pontifícia universidade católica, Rio de Janeiro, 2016.
[62]Y. Jodai and G. E. Elsinga, "Experimental observation of hairpin autogeneration events in a turbulent boundary layer," J. Fluid Mech. **795**, 611–633 (2016).
[63]T. A. Earl, S. Cochard, B. Tremblais, L. Thomas, and L. David, "Evaluation of the energy dissipation from tomographic PIV measurements in an open channel flow behind regular grids," in *Proceedings of the 35th IAHR World Congress* (Tsinghua University Press, 2013), pp. 8–13.
[64]A. Schröder, D. Schanz, C. Roloff, and D. Michaelis, "Lagrangian and Eulerian dynamics of coherent structures in turbulent flow over periodic hills using time-resolved tomo PIV and 4D-PTV 'shake-the-box,'" *Presented at the 17th International Symposium on Applications of Laser Techniques to Fluid Mechanics*, Lisbon, Portugal, 7-10 July 2014, pp. 07–10, https://www.researchgate.net/publication/263889492.
[65]G. E. Elsinga, F. Scarano, B. Wieneke, and B. W. van Oudheusden, "Tomographic particle image velocimetry," Exp. Fluids **41**, 933–947 (2006),
[66]M. Virant and T. Dracos, "3D PTV and its application on Lagrangian motion," Meas. Sci. Technol. **8**, 1539 (1997).
[67]L. Schaefer, U. Dierksheide, M. Klaas, and W. Schroeder, "Investigation of dissipation elements in a fully developed turbulent channel flow by tomographic particle-image velocimetry," Phys. Fluids **23**, 035106 (2011).
[68]D. Schanz, S. Gesemann, and A. Schröder, "Shake-the-box: Lagrangian particle tracking at high particle image densities," Exp. Fluids **57**, 70 (2016).
[69]M. Kind and H. Martin, *VDI-Wärmeatlas* (Springer, 2013).
[70]NI Core Team, Implementing the PID Algorithm with the PID VIs, National Instruments Corporation, 2022.
[71]K. J. Åström and T. Hägglund, "Automatic tuning of simple regulators," IFAC Proc. Vol. **17**, 1867–1872 (1984).
[72]S. Pirozzoli, "On turbulent friction in straight ducts with complex cross-section: The wall law and the hydraulic diameter," J. Fluid Mech. **846**, R1 (2018).
[73]L. Schiller, "Über den strömungswiderstand von rohren verschiedenen querschnitts und rauhigkeitsgrades," Z. Angew. Math. Mech. **3**, 2–13 (1923).
[74]S. B. Pope, *Turbulent Flows* (IOP Publishing, 2001).
[75]M. P. Schultz and K. A. Flack, "Reynolds-number scaling of turbulent channel flow," Phys. Fluids **25**, 025104 (2013).
[76]J. Monty and M. Chong, "Turbulent channel flow: Comparison of streamwise velocity data from experiments and direct numerical simulation," J. Fluid Mech. **633**, 461–474 (2009).
[77]F.-C. Li, Y. Kawaguchi, T. Segawa, and K. Hishida, "Reynolds-number dependence of turbulence structures in a drag-reducing surfactant solution channel flow investigated by particle image velocimetry," Phys. Fluids **17**, 075104 (2005).
[78]M. A. Niederschulte, R. J. Adrian, and T. J. Hanratty, "Measurements of turbulent flow in a channel at low Reynolds numbers," Exp. Fluids **9**, 222–230 (1990).
[79]P. Costa, "A FFT-based finite-difference solver for massively-parallel direct numerical simulations of turbulent flows," Comput. Math. Appl. **76**, 1853–1862 (2018).
[80]R. D. Moser, J. Kim, and N. N. Mansour, "Direct numerical simulation of turbulent channel flow up to $Re_\tau = 590$," Phys. Fluids **11**, 943–945 (1999).
[81]M. Bernardini, S. Pirozzoli, and P. Orlandi, "Velocity statistics in turbulent channel flow up to $Re_\tau \approx 4000$," J. Fluid Mech. **742**, 171–191 (2014).
[82]M. Lee and R. Moser, "Direct numerical simulation of turbulent channel flow up to $Re_\tau \approx 5200$," J. Fluid Mech. **774**, 395–415 (2015).
[83]M. Atzori, R. Vinuesa, A. Lozano-Durán, and P. Schlatter, "Intense Reynolds-stress events in turbulent ducts," Int. J. Heat Fluid Flow **89**, 108802 (2021).
[84]D. Modesti, S. Pirozzoli, P. Orlandi, and F. Grasso, "On the role of secondary motions in turbulent square duct flow," J. Fluid Mech. **847**, R1 (2018).
[85]R. Vinuesa, A. Noorani, A. Lozano-Durán, G. K. E. Khoury, P. Schlatter, P. F. Fischer, and H. M. Nagib, "Aspect ratio effects in turbulent duct flows studied through direct numerical simulation," J. Turbul. **15**, 677–706 (2014).
[86]R. J. Moffat, "Describing the uncertainties in experimental results," Exp. Therm. Fluid Sci. **1**, 3–17 (1988).
[87]Endress + Hauser, Technical Information: Proline Promag 10D, 2018.
[88]T. Astarita and G. Cardone, "Analysis of interpolation schemes for image deformation methods in PIV," Exp. Fluids **38**, 233–243 (2005).
[89]T. Astarita, "Analysis of weighting windows for image deformation methods in PIV," Exp. Fluids **43**, 859–872 (2007).
[90]T. Astarita, "Adaptive space resolution for PIV," Exp. Fluids **46**, 1115–1123 (2009).
[91]R. Moser, J. Kim, and N. Mansour, DNS data for turbulent channel flow, 1999, data retrieved from https://turbulence.oden.790utexas.edu/MKM_1999.html.
[92]J. Kim, P. Moin, and R. Moser, "Turbulence statistics in fully developed channel flow at low Reynolds number," J. Fluid Mech. **177**, 133–166 (1987).
[93]A. Sciacchitano, B. Wieneke, and F. Scarano, "PIV uncertainty quantification by image matching," Meas. Sci. Technol. **24**, 045302 (2013).
[94]A. Sciacchitano, Webpage Url: PIV Uncertainty Code, 2015.
[95]A. Sciacchitano and B. Wieneke, "PIV uncertainty propagation," Meas. Sci. Technol. **27**, 084006 (2016).
[96]W. Abu Rowin, J. Hou, and S. Ghaemi, "Turbulent channel flow over riblets with superhydrophobic coating," Exp. Therm. Fluid Sci. **94**, 192–204 (2018).
[97]A. Kendall and M. Koochesfahani, "A method for estimating wall friction in turbulent wall-bounded flows," Exp. Fluids **44**, 773–780 (2008).

[98]H. M. Nagib and K. A. Chauhan, "Variations of von Kármán coefficient in canonical flows," Phys. Fluids **20**, 101518 (2008).
[99]S. Heinz, "On mean flow universality of turbulent wall flows. I. High Reynolds number flow analysis," J. Turbul. **19**, 929–958 (2018).
[100]L. Prandtl, "Eine beziehung zwischen warmeaustausch and stromungswiderstand der flussigkeiten," Phys. Z. **11**, 1072–1078 (1910).
[101]H. M. Nagib, K. A. Chauhan, and P. A. Monkewitz, "Approach to an asymptotic state for zero pressure gradient turbulent boundary layers," Philos. Trans. R. Soc., A **365**, 755–770 (2007).
[102]G. I. Taylor, "Conditions at the surface of a hot body exposed to the wind," Rep. Mem. Br. Advis. Comm. Aeronaut. **272**, 423–429 (1916).
[103]D. Coles, "The young person's guide to the data," in *Technical Report No. AD0695076* (RAND Corp, Santa Monica, CA, 1968).
[104]R. Örlü, J. H. Fransson, and P. Henrik Alfredsson, "On near wall measurements of wall bounded flows—The necessity of an accurate determination of the wall position," Prog. Aerosp. Sci. **46**, 353–387 (2010).
[105]W. K. George, "Is there a universal log law for turbulent wall-bounded flows?," Philos. Trans. R. Soc., A **365**, 789–806 (2007).
[106]M. H. Buschmann and M. Gad-el Hak, "Recent developments in scaling of wall-bounded flows," Prog. Aerosp. Sci. **42**, 419–467 (2006).
[107]I. Marusic, B. J. McKeon, P. A. Monkewitz, H. M. Nagib, A. J. Smits, and K. R. Sreenivasan, "Wall-bounded turbulent flows at high Reynolds numbers: Recent advances and key issues," Phys. Fluids **22**, 065103 (2010).
[108]B. J. Mckeon, J. Li, W. Jiang, J. F. Morrison, and A. J. Smits, "Further observations on the mean velocity distribution in fully developed pipe flow," J. Fluid Mech. **501**, 135–147 (2004).
[109]A. E. Perry, S. Hafez, and M. S. Chong, "A possible reinterpretation of the Princeton superpipe data," J. Fluid Mech. **439**, 395–401 (2001).
[110]M. V. Zagarola and A. J. Smits, "Mean-flow scaling of turbulent pipe flow," J. Fluid Mech. **373**, 33–79 (1998).
[111]J. P. Monty, N. Hutchins, H. C. H. Ng, I. Marusic, and M. S. Chong, "A comparison of turbulent pipe, channel and boundary layer flows," J. Fluid Mech. **632**, 431–442 (2009).
[112]MATLAB, version 9.13.0 (R2022b), Natick, MA, 2022.
[113]A. U. M. Masuk, A. Salibindla, and R. Ni, "A robust virtual-camera 3D shape reconstruction of deforming bubbles/droplets with additional physical constraints," Int. J. Multiphase Flow **120**, 103088 (2019).
[114]B. Wieneke, "Volume self-calibration for 3D particle image velocimetry," Exp. Fluids **45**, 549–556 (2008).